

1-1-2003

## A numerical study of fire spread phenomena for multi-level apartment complexes

John Howard Mammoser III  
*Iowa State University*

Follow this and additional works at: <https://lib.dr.iastate.edu/rtd>

### Recommended Citation

Mammoser, John Howard III, "A numerical study of fire spread phenomena for multi-level apartment complexes" (2003). *Retrospective Theses and Dissertations*. 19496.  
<https://lib.dr.iastate.edu/rtd/19496>

This Thesis is brought to you for free and open access by the Iowa State University Capstones, Theses and Dissertations at Iowa State University Digital Repository. It has been accepted for inclusion in Retrospective Theses and Dissertations by an authorized administrator of Iowa State University Digital Repository. For more information, please contact [digirep@iastate.edu](mailto:digirep@iastate.edu).

**A numerical study of fire spread phenomena for multi-level apartment  
complexes**

by

John Howard Mammoser III

A thesis submitted to the graduate faculty  
in partial fulfillment of the requirements for the degree of  
MASTER OF SCIENCE

Major: Mechanical Engineering

Program of Study Committee:  
Francine Battaglia, Major Professor  
Theodore Heindel  
John C. Tannehill

Iowa State University

Ames, Iowa

2003

Copyright © John Howard Mammoser III, 2003. All rights reserved.

Graduate College  
Iowa State University

This is to certify that the master's thesis of  
John Howard Mammoser III  
has met the thesis requirements of Iowa State University

Signatures have been redacted for privacy

---

## TABLE OF CONTENTS

<b>LIST OF TABLES</b> . . . . .	v
<b>LIST OF FIGURES</b> . . . . .	vi
<b>NOMENCLATURE</b> . . . . .	ix
<b>DEDICATION</b> . . . . .	xiii
<b>ACKNOWLEDGMENTS</b> . . . . .	xiv
<b>ABSTRACT</b> . . . . .	xv
<b>1 INTRODUCTION</b> . . . . .	1
<b>2 LITERATURE REVIEW</b> . . . . .	6
2.1 Physics of Fire . . . . .	6
2.2 Building Fires . . . . .	8
2.3 Computational Fire Models . . . . .	14
2.3.1 Zone Models . . . . .	15
2.3.2 Field Models . . . . .	17
<b>3 METHODOLOGY</b> . . . . .	19
3.1 Governing Equations . . . . .	19
3.2 Mixture Fraction Combustion Model . . . . .	21
3.3 Radiation Model . . . . .	22
3.4 Numerical Formulation . . . . .	23

<b>4</b>	<b>RESULTS</b>	<b>27</b>
4.1	Combustion Validation	27
4.2	Building Geometry	29
4.2.1	Boundary and Initial Conditions	32
4.2.2	Grid Resolution	33
4.3	Scaling Laws	33
4.4	Effect of Balcony Depth	36
4.5	Effect of Balcony Geometry	40
4.5.1	Boundary Conditions for Balustrades	40
4.5.2	Comparison of Balcony Types	42
4.6	Wind Effects	46
4.6.1	Building Geometry	46
4.6.2	Boundary and Initial Conditions	46
4.6.3	Scaling Laws for Wind	46
4.6.4	Wind Impinging on a High Rise Building with Balconies	47
<b>5</b>	<b>CONCLUSIONS</b>	<b>52</b>
	<b>BIBLIOGRAPHY</b>	<b>54</b>

## LIST OF TABLES

Table 4.1	Constants in McCaffrey correlations for a 16 kW propane fire. . . . .	28
Table 4.2	Comparison of model to full scale heat release rates. . . . .	35
Table 4.3	Definitions for various complex balcony geometries. . . . .	42
Table 4.4	Comparison of full to model scale wind velocities. . . . .	48

## LIST OF FIGURES

Figure 1.1	Schematic of a compartment for the two-zone model. . . . .	3
Figure 2.1	Schematic of a candle flame. . . . .	7
Figure 2.2	Schematic of an apartment complex depicting the location of the balcony and spandrel. . . . .	9
Figure 2.3	Schematic of burn room with variable window sizes for Oleszkiewicz [36]. . . . .	11
Figure 2.4	Details of fire room with (a) horizontal and (b) vertical projections for Oleszkiewicz [37]. . . . .	11
Figure 2.5	Schematic of building with horizontal projection for Galea et al. numerical study [39]. . . . .	12
Figure 2.6	(a) Schematic of building geometry and (b) enlargement of fire room geometry for the 1/7 scale experiment for Suzuki et al. [40].	13
Figure 2.7	Detail of burn room geometry for 1/3 scale model with separation walls and balustrade for Suzuki et al. [41]. . . . .	15
Figure 3.1	Schematic of a computational cell showing velocity vector quantities. . . . .	24
Figure 3.2	Schematic of a wall and ghost cell at a solid wall or boundary. . . . .	26
Figure 4.1	Comparison of McCaffrey correlations with LES for the time-averaged centerline (a) temperature and (b) vertical velocity. . . . .	29

Figure 4.2	Schematic of apartment building, illustrating which portion was numerically simulated. . . . .	30
Figure 4.3	Schematic of apartment complex and fire room for (a) cross-section view, and (b) top view. . . . .	31
Figure 4.4	Average exterior wall temperatures versus wall height for a 48 kW propane fire and 17.5 cm BD for grid resolution study. . . . .	34
Figure 4.5	Average exterior wall temperatures versus wall height comparing a full scale 6.22 MW fire versus 1/7th scale 48 kW fire. . . . .	35
Figure 4.6	Average temperature contours for a 48 kW propane fire for balcony depths of (a) 0 cm, (b) 10 cm, (c) 15 cm, (d) 17.5 cm and (e) 20 cm. . . . .	38
Figure 4.7	Average exterior wall temperatures versus wall height for a 48 kW propane fire. . . . .	38
Figure 4.8	Average exterior wall temperatures versus wall height for a 95 kW propane fire. . . . .	39
Figure 4.9	Balcony Configurations: (a) Type I, (b) Type II, (c) Type III, (d) Type IV (Photos by author). . . . .	41
Figure 4.10	Average temperature contours for a 48 kW propane fire for balcony Types (a) I, (b) II), (c) III and (d) IV with BD=17.5 cm. . . . .	44
Figure 4.11	Average exterior wall temperatures versus wall height for a 48 kW propane fire for Types I–IV balconies. . . . .	44
Figure 4.12	Instantaneous room temperature for a 48 kW propane fire for Types I–IV balconies with a 17.5 cm BD. . . . .	45
Figure 4.13	Schematic of a top view of an apartment complex and fire room for $\theta = 45^\circ$ wind simulations. . . . .	47

Figure 4.14 Instantaneous temperature contours at  $t=48$  s and wind angle  $\theta=45^\circ$  at locations (a)  $y=0.48$  m, (b)  $y=0.71$  m, (c)  $y=0.77$  m, (d)  $y=0.83$  m, (e)  $y=0.89$  m and (f)  $y=0.93$  m. . . . . 50

Figure 4.15 Instantaneous temperature contours at  $t=48$  s and wind angle  $\theta=45^\circ$  at locations (a)  $x=-0.015$  m, (b)  $x=-0.045$  m, (c)  $x=-0.075$  m, (d)  $x=-0.105$  m, (e)  $x=-0.135$  m and (f)  $x=-0.180$  m. . . . . 51

## NOMENCLATURE

$C_s$	empirical constant for Smagorinsky model
$c_{p,i}$	constant pressure specific heat of $i$ th species
$D$	total diffusion coefficient
$D_h$	hydraulic diameter at flame base
$D_i$	diffusion coefficient of $i$ th species
$F_n$	normal component of $\mathbf{f}$
$\mathbf{f}$	external force vector (excluding gravity)
$\mathbf{g}$	gravity vector
$\mathcal{H}$	pressure head
$h$	total enthalpy
$h_i$	enthalpy of $i$ th species
$I_{b,n}$	blackbody radiation intensity over band $n$
$I_n$	radiation intensity over band $n$
$k$	thermal conductivity
$L$	length of flame
$M_i$	molecular weight of $i$ th species
$p$	pressure
$p_o$	background pressure
$\tilde{p}$	perturbation pressure
$\dot{Q}$	heat release rate (kW)

$q'''$	heat release rate per unit volume
$\mathcal{R}$	universal gas constant
$S$	deformation tensor
$\hat{s}$	unit normal direction vector
$T$	temperature
$t$	time
$\mathbf{u}$	velocity vector $(u, v, w)$
$\dot{W}_i'''$	production rate of $i$ th species per unit volume
$\mathbf{x}$	position vector $(x, y, z)$
$Y_F^I$	fuel stream mass fraction
$Y_i$	mass fraction of $i$ th species
$Y_O^\infty$	ambient oxygen mass fraction
$Z$	mixture fraction

## Greek Symbols

$\gamma$	ratio of specific heats
$\Delta$	filter width; change
$\eta$	McCaffrey constant
$\kappa$	absorption coefficient
$\mu$	dynamic viscosity
$\nu$	stoichiometric coefficient for overall combustion reaction
$\rho$	density
$\sigma$	Stefan-Boltzmann constant
$\tau$	viscous stress tensor
$\chi_r$	radiative fraction loss

$\omega$  vorticity vector

## Superscripts

$n$  time step

## Subscripts

$e$  estimate

$F$  fuel

$f$  full scale

$i$   $i$ th species

$i, j, k$  computational cell indices

$\infty$  ambient

$m$  model scale

$n$  spectral band

$O$  oxygen

## Other Symbols

$\nabla$  gradient operator

$\nabla \cdot$  divergence operator

## Abbreviations

BD	balcony depth
CFD	computational fluid dynamics
CFL	Courant-Fredrichs-Lewy number
DNS	direct numerical simulation
FDS	fire dynamics simulator
FF	fire floor
FF +1	one floor above the fire floor
FF +2	two floors above the fire floor
LES	large eddy simulation
NIST	National Institute of Standards and Technology
RANS	Reynolds averaged Navier-Stokes equations
RTE	radiation transport equation

## DEDICATION

-For Monga, my grandmother from Ireland, who understood the value of education, despite only having a 4th grade education herself.

## ACKNOWLEDGMENTS

I would like to take this opportunity to thank those people who have helped me achieve success in education and life.

I would first like to thank Dr. Francine Battaglia for seeing something in me which I could not see myself. I am forever indebted to her for the guidance she gave me in my last year as an undergraduate and her encouragement for me to attend graduate school. During my graduate program, she helped to guide my research as well as give insight with my work which I had not seen. To the other members of my committee, Dr. Theodore Heindel, for his guidance with heat transfer and Dr. John C. Tannehill, for his excellent instruction in computational fluids.

To my family, who provided emotional and financial support for my educational goals. To my mother Kay, who has spent most of my lifetime helping correct my written and spoken English grammar. To my father John II, who helped develop my logic and mathematical skills at an early age. To my brother Kevin, who still finds a way to keep me grounded despite not understanding most of what my research involves. To the love of my life, my wife Laura, for all her understanding and support over the past several years. She has truly been my strength and sanity while in graduate school.

And last but not least, to my friends and colleagues in the basement CFD office: Farshid, Anup, Nan, Jin, Andrew, Xiaofeng, Joon, Chunjian (Charles), Kunlun (Mao), Xiaohang, Zhaohui, Ying, Madhusudan, Hong, Yang, Ravi and Steve. The open discussions and free flow of ideas about CFD, mathematics, politics and life make our office a great place to learn and exemplifies the ideal graduate experience.

## ABSTRACT

High rise apartment fires are perhaps the most dangerous residential fires. Within high rise buildings, flames and smoke can travel through ductwork, between interior walls, and up elevator shafts and stairwells. One of the fastest ways a fire spreads to other floors is along the exterior of the building due to open windows. Flame spread up vertical walls has been studied experimentally and computationally for years in the U.S. and abroad. Preventing or reducing fire spread on the exterior of buildings allows fire fighters more time to evacuate the occupants above the fire, and more time to control the fire from spreading to other floors or neighboring buildings.

A numerical study has been undertaken to examine the reduction of vertical flame spread due to the presence of a balcony. The Fire Dynamics Simulator (FDS) code developed at the National Institute of Standards and Technology will be used to determine how balconies affect the vertical movement of fire. The FDS large eddy simulation methodology coupled with a mixture fraction combustion model will be tested. Implementing building geometry from scaled experiments, the computational study will vary balcony depth and geometry, in an effort to find an optimum balcony depth and configuration that significantly impedes vertical fire spread on the external wall. Wind impinging on the facade of the building will be introduced at various angles to determine what affect wind may have on fire spread in high rise buildings.

## CHAPTER 1 INTRODUCTION

The discovery of fire thousands of years ago has had a profound affect on the world. Fire has allowed humans to make great advances in science, such as the development and use of the internal combustion engine, and propulsion systems to travel several times faster than the speed of sound. Fire has also brought civilization to its knees such as the Great Chicago Fire of 1871 [1] and recently the disaster of the World Trade Center [2] and the Pentagon [3] in 2001. While these examples of fire disasters are well known, fires occur on a daily basis. One such example is an apartment building fire which can also have devastating effects. Within high rise buildings, flames and smoke can travel through ductwork, between interior walls, and up elevator shafts and stairwells. Lives can be lost (occupants and fire fighters alike) and damage can be permanent, disrupting and displacing families.

According to the U.S. Fire Administration, from 1996 to 1998, there were an estimated 15,500 high rise fires in the United States [4] and three quarters of these fires were residential structures. Over two thirds of high rise fires originate at or below the fourth floor level, that is below 50 feet. Most high rise fires start low in the building structure, increasing the chances for the fire to spread vertically along the exterior surface of the building. While these residential high rise fires are not monetarily costly compared to commercial high rise fires, they do cost lives, more so than all other structural fires [4].

Research must be devoted to help in the prevention of fire disasters from overshadowing advances in the use of fire and combustion. Large fire disasters occur when the spread of fire and smoke surpasses the rate at which the fire can be contained as well

as the rate at which people can evacuate. Therefore, researching ways to minimize the damaging effects of fire and smoke spread will undoubtedly benefit society in the reduction of fatalities.

The study of fire and how it spreads has started an entirely new area of research called fire dynamics: the kinetics of combustion and fluid movement in urban or environmental settings. To investigate large-scale fire phenomena such as buildings [5,6] or forest fires [7,8], experimental [9–11] and computational [12–14] approaches have been instrumental in advancing our understanding of how fires spread. Both approaches have strengths and weaknesses. For example, full-scale experimental models provide the most realistic scenario. However, it is not always feasible to perform a burn on an urban building. Small scale experimental models can be tested in a laboratory, but the difficulty lies in determining the proper scaling laws [15–17]. Experiments can also be very expensive to build and can be ruined after a single test, thus no longer useful for further experiments. An additional difficulty with experiments is that it is challenging to insert a probe in a fire without damaging the probe [18] or avoiding particulates from aggregating on the probe tip and distorting the accuracy of the measurement [19]. Non-intrusive instruments are an alternative means to conduct measurements but there are also limitations such as illuminating a laser sheet in a fire [20,21].

Computational fluid dynamics (CFD) offers an alternative means to study fluid movement and combustion. One advantage is that computations can provide data often difficult to obtain experimentally due to the limitations of experimental equipment. There are two main challenges with computations. The first is developing models to accurately represent the physics of the problem under investigation. For example, to simulate a fire requires numerical resolution of large and small length and time scales; however, there is a large disparity between these scales associated with the hydrodynamics and combustion [22]. In order to resolve all the scales, appropriate modeling is required as well as adequate computational resources, leading to the second challenge: computa-

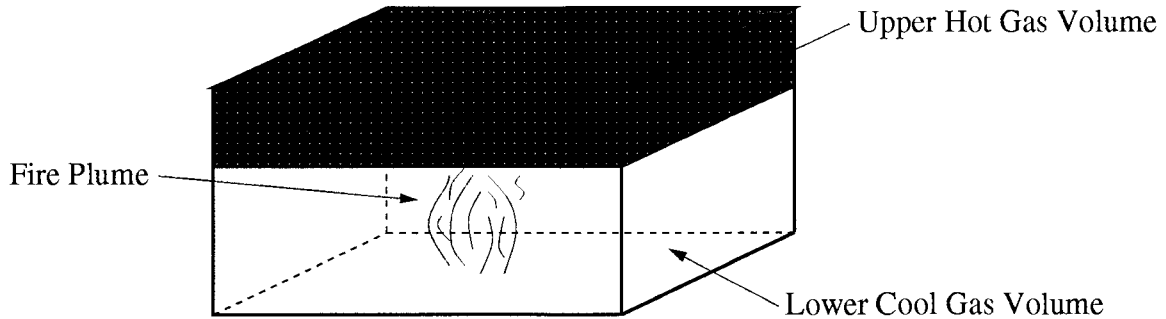


Figure 1.1 Schematic of a compartment for the two-zone model.

tional power. Recently, advances in computational speed, processors and memory have allowed for three-dimensional CFD modeling of fires.

Great strides have been made over the years to develop and improve models to best represent fire dynamics. The two most common CFD fire models are the *zone* models and *field* models. *Zone* models consider the fire compartment, and provide a way to interconnect different zones, where each zone represents a unique computational space. The most common zone model is the two-zone model, which contains two distinct volumes: an upper hot gas and a lower cool gas volume (see Fig. 1.1). The semi-empirical equations for mass, momentum, energy and species are solved separately for each volume [23]. The fire plume itself is a source of mass and energy, and acts as a “pump” to transfer mass from the lower to the upper zone through entrainment [24]. However, zone models should only be used to find approximate gas temperatures and location of the smoke layer.

*Field* models are based on solving the Navier-Stokes equations. Examples of field models are the Reynolds-averaging technique for Navier-Stokes equations (RANS), the  $k - \epsilon$  turbulence model summarized by Patankar [25], and large eddy simulation (LES) methodology, all of which allow for modeling of more complex fire scenarios. The RANS and  $k - \epsilon$  models are time averaging techniques and have an undesirable effect of smoothing the results. An alternative to the  $k - \epsilon$  model is large eddy simulation. The LES

technique assumes large scale eddies account for the majority of turbulent mixing effects, and thus the small scale eddies are either approximated or ignored. The approximation of small scale effects does not sufficiently capture the physics of combustion and pyrolysis, which occur at small length scales, less than 1 mm. A modified approach uses a “low Mach number” formulation [26] along with LES techniques. The benefit is that a course mesh can be used and still attain accurate results.

The Fire Dynamics Simulator (FDS) code used in this investigation was developed at the National Institute of Standards and Technology (NIST) by McGrattan et al. [22] and is a LES-based field model code. The large-scale physics are simulated directly and the small scale effects are represented using a Smagorinsky model for turbulence. Combustion is simulated using a mixture fraction model, while radiation is calculated using a radiation transport equation (RTE) for a non-scattering gray gas, such that the gas behaves as a gray medium and that soot is the primary combustion product controlling thermal radiation. The governing equations are discretized with second-order central differencing, and solved on a Cartesian grid. A second-order accurate Runge-Kutta scheme is used to advance the velocity and temperature fields. The Poisson equation for pressure is solved directly using fast Fourier transforms and block tri-diagonal solvers. Further details can be found in [22].

The motivation of this research is to computationally investigate fires ejecting from an opening of a multi-story building to determine how balcony depth affects the flow of hot gases. The secondary objective of this study is to find an optimal balcony geometry (e.g., depth, balustrade and privacy wall configurations) that best impedes the vertical spread of fires. The thesis is laid out as follows. First, Chapter 2 will review the physical process of fire and combustion, vertical fire spread experiments and computational research from the past several decades, and the difficulties in numerically simulating fire. The governing equations, combustion and radiation models, and the numerical formulation behind the FDS code will be discussed in Chapter 3. Chapter 4 presents the geometry, boundary

conditions, validation and discussion of results for varying balcony depths and balcony geometries. Finally, wind impinging on the facade of the building will be introduced at various angles to determine what affect wind may have on fire spread in high rise buildings.

## CHAPTER 2 LITERATURE REVIEW

### 2.1 Physics of Fire

Fire is a complex physical and chemical process and is often best illustrated using the example of a candle, as suggested by Faraday in his “Christmas Lectures” at the Royal Institute in London [27]. When a source of ignition is placed close to the wick, the solid wax melts and soon evaporates. The gaseous wax moves by diffusion into a region with a large oxygen concentration. A set of complex chemical reactions oxidizes the gas which then ignites into a flame. The flame radiates heat back to the solid wax, which soon melts. The liquid wax is drawn up the wick to the flame by capillary action. A continuous process of melting, vaporizing and burning creates a stable flame [24]. Figure 2.1 illustrates this process. If any one fundamental component such as radiant heat, oxygen or fuel, is removed from the process, the flame will self extinguish, not only with a candle, but also with large building fires or forest fires. Inadequate amounts of oxygen or fuel will cause the flame to “wander”. Understanding how fires spread can help to better illustrate this idea of a “wandering” flame.

While the fuel for a candle flame is transported to the combustion region through the wick, a fire burning on a chair, couch, bed or tree will “move” or spread to where more fuel is available. The direction of flame spread will depend on whether horizontal or vertical convective movement dominates. Horizontal flame movement can result from forced air flows, while vertical movement can result from the buoyant flow of hot gases from the flame. Buoyant heat flow can cause a rapid increase in vertical fire propagation [28].

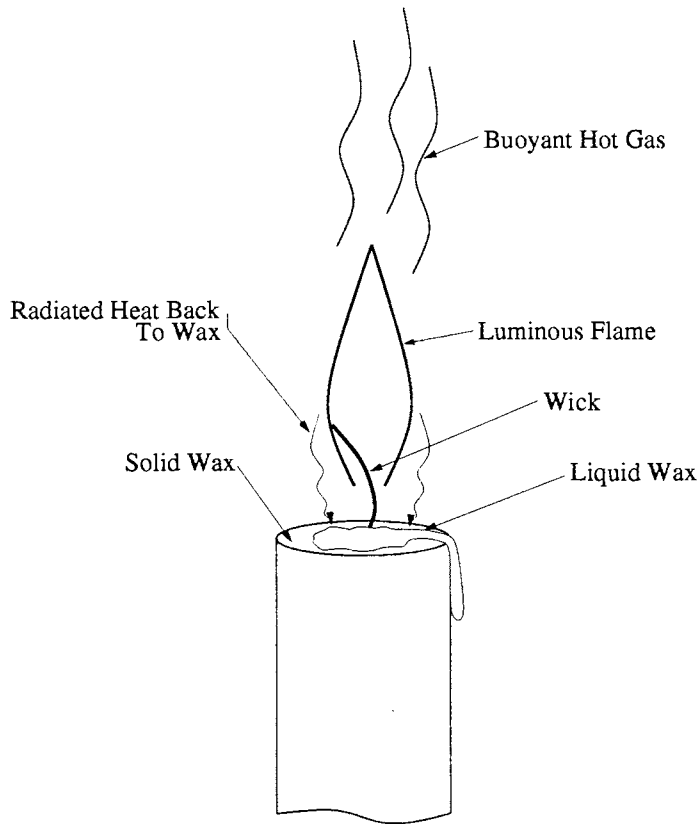


Figure 2.1 Schematic of a candle flame.

The sustained vertical propagation of fire along a wall is determined by several important factors. The radiation from an attached flame pre-heats the combustible wall materials to the pyrolysis temperature before ignition. Depending on the material, the initial attached flame may not provide enough radiation to sustain combustion. External radiation from flames not directly involved can aid in the propagation of flame spread. According to Brebob and Kulkarni [29], external radiant heat to the unburned region of a material adds to the heat provided by the attached flame and decreases the pyrolysis time. The external radiation also increases the mass loss rate of material already consumed in flames, creating a larger flaming region. Therefore, impeding or preventing flame spread is of the utmost importance for everyone's safety.

Preventing or reducing fire spread on the exterior of buildings allows fire fighters more

time to evacuate the occupants above the fire floor, and more time to control the fire from spreading to other floors or neighboring buildings. Numerical and experimental research has indicated that external fire spread commonly travels vertically through window openings [30–33]. Research has also shown that radiation from fire through window openings can cause ignition of materials on neighboring buildings [34]. Yokoi's [35] experimental work in 1960 revealed that a 0.74 m horizontal projection perpendicular to the wall above a window prevented the glass window above the projection from breaking. These findings led to building code changes in Japan, requiring some structures to have horizontal projections, called “eyebrows”, equivalent to today's balconies.

## 2.2 Building Fires

The balcony is a horizontal projection perpendicular to the exterior of a vertical wall, and the balcony depth is the distance the balcony protrudes from the wall, as shown in Fig. 2.2. The spandrel is the vertical distance between window or door openings from one floor to the floor above. Without the presence of a balcony, a fire projecting from a window tends to travel vertically, unobstructed along the wall. However, the presence of the balcony can deflect a flame outward, away from the wall, thus impeding the vertical fire spread and reducing radiation to the floors above. The key to impeding vertical fire spread is in preventative measures such as the window and balcony geometry.

In the past few decades, the size and location of windows and balconies have regained interest based on several significant high rise fires. At the National Research Council of Canada, Oleszkiewicz [36] experimentally investigated the effect of window geometry using a test facility of concrete blocks covered with non-combustible wallboard and one window opening. The test facility measured 10.3 m tall by 6.0 m wide by 4.5 m deep, and the 2.75 m high room where the fire originated was located at the ground level (see Fig. 2.3). The window located on the facade ranged in height and width

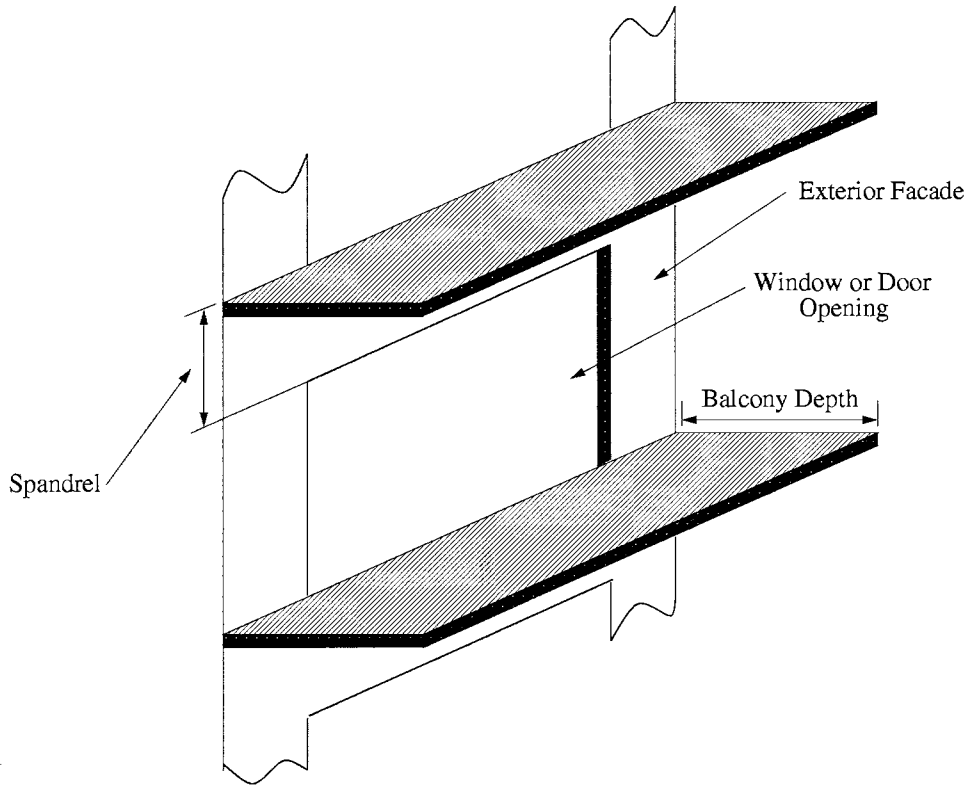


Figure 2.2 Schematic of an apartment complex depicting the location of the balcony and spandrel.

with a minimum height of 1.37 m and a maximum width of 2.6 m. The wall above the window opening was lined with non-combustible wall board (Marinite). The fire room contained four propane diffusion burners, equally spaced, providing a 6 MW fire. Experiments were conducted to determine how window size affected the flame exposure to the facade. Results showed that a very low-height and wide window produced the most flame exposure to the wall above, while a relatively square window reduced the flame exposure. The hot gases passing through the low, wide window opening had lower velocities and the flames attached to the wall more easily than with a tall, narrow window opening.

Oleszkiewicz [37] also investigated the effects of horizontal and vertical projections on vertical fire spread. In a 1.13 m square test facility, a 1.22 m deep and 2.44 m

wide horizontal projection was placed directly over the window opening (Fig. 2.4(a)). Another test placed 1.22 m deep vertical projections along both sides of the windows (Fig. 2.4(b)). The horizontal projection decreased the heat flux to the wall above the opening by 90%, whereas the vertical projections increased the heat flux by 50%. The significance of the heat flux study is that fluxes as low as  $12.5 \text{ kW/m}^2$  have been shown to ignite ordinary combustible material [37]. These tests illustrate the effectiveness of horizontal projections in decreasing the heat flux to the surface above the window opening.

Another experiment by Oleszkiewicz [38] investigated the effect of spandrel distance (refer to Fig. 2.2). Oleszkiewicz found that increasing the spandrel could significantly reduce vertical fire spread. The increased spandrel distance allows the hot gases ejecting from an opening to cool as it rises, thus reducing the heat flux to the facade above. However, increasing the spandrel proved to be impractical. For example, Oleszkiewicz found that to achieve a 50% reduction in heat flux above an opening, a 2.5 m spandrel would be required, which is much larger than most building code requirements.

In the mid-1990's, Galea, et al. [39] used a commercial numerical code (FLOW3D) to model the effects of window geometry and horizontal projections on vertical flame spread. An eight-story building was modeled with dimensions of 22.8 m high by 22 m wide by 16.8 m deep as shown in Fig. 2.5. The test fire room was located on the third floor with dimensions of 2.5 m high by 4 m wide by 4.75 m deep. The window opening was varied in height and width, from a tall, narrow window to a low, wide window. A 1 m horizontal projection was also used in some cases. A 1 MW heat source was centrally located within the room. Galea et al. [39] showed that a low, wide window induced the flame to attach to the wall above, agreeing with Oleszkiewicz's experimental work [36]. Galea et al. also showed that placing a 1 m horizontal projection perpendicular to the wall above the window allowed the flame to detach itself from the wall for a short period of time before re-attaching, significantly reducing the temperatures along the wall.

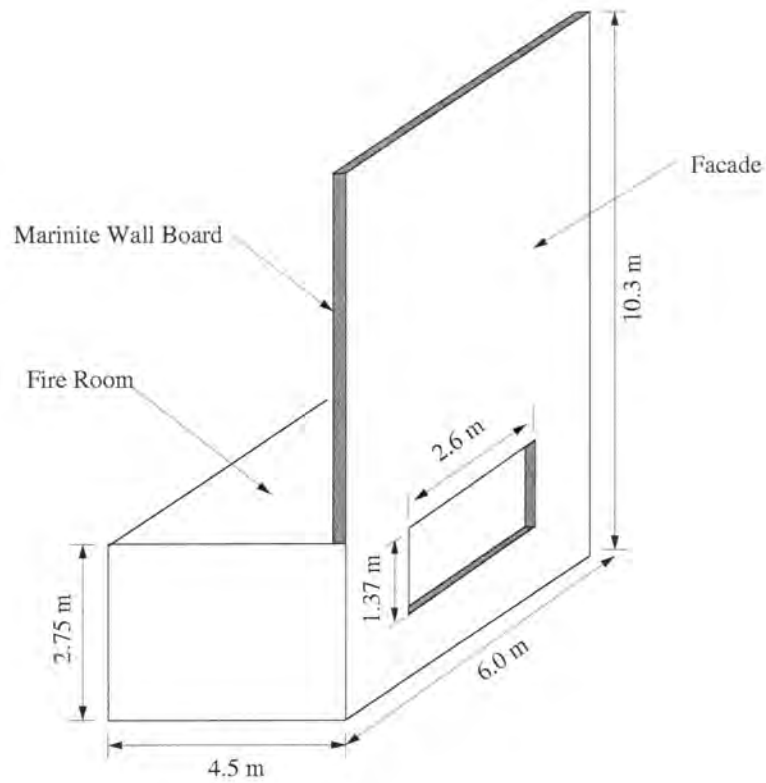


Figure 2.3 Schematic of burn room with variable window sizes for Oleszkiewicz [36].

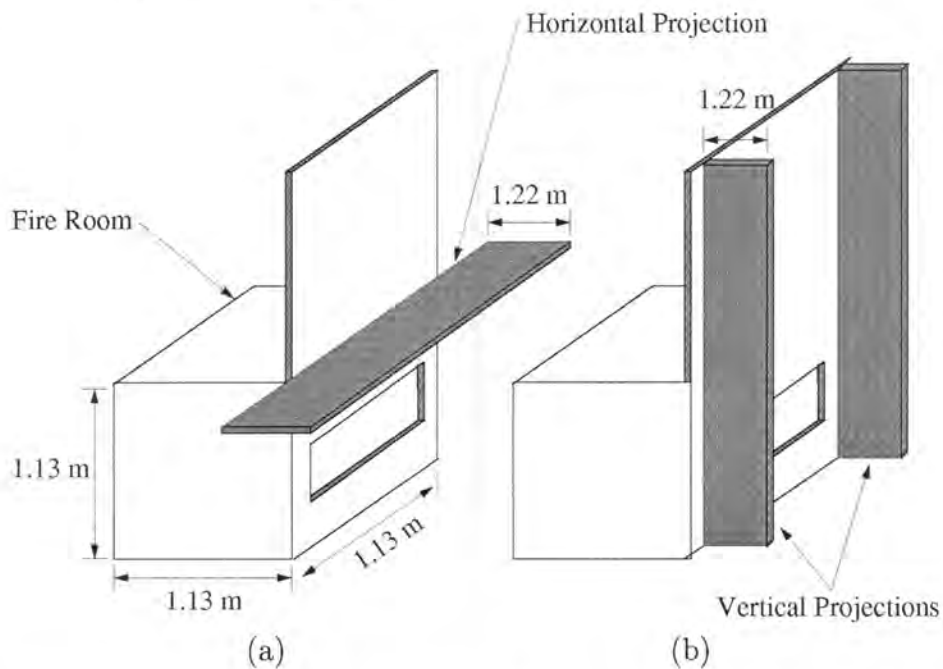


Figure 2.4 Details of fire room with (a) horizontal and (b) vertical projections for Oleszkiewicz [37].

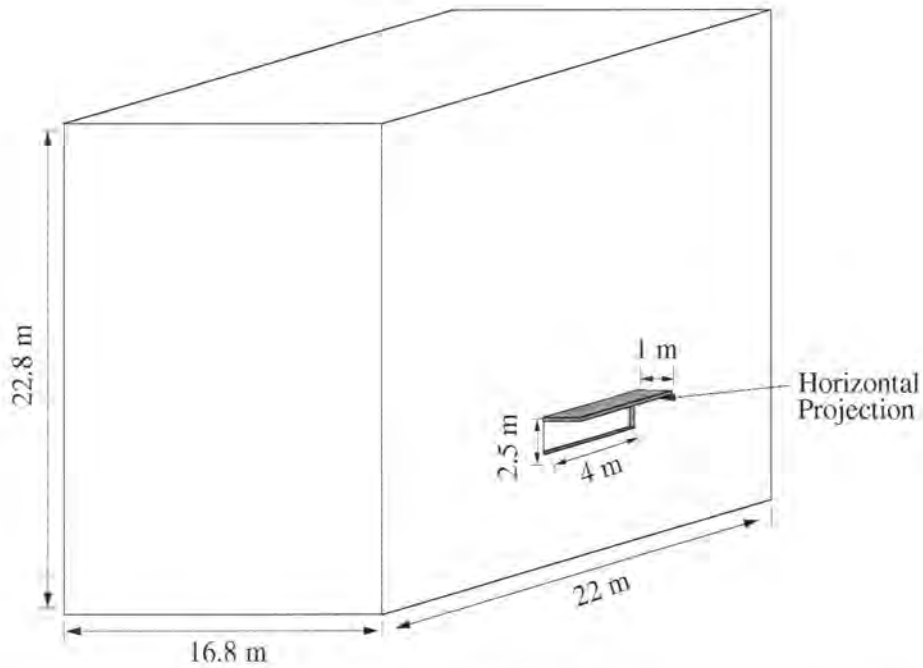


Figure 2.5 Schematic of building with horizontal projection for Galea et al. numerical study [39].

Recently, researchers from the National Research Institute of Fire and Disaster in Japan completed several experimental studies on the effects of balconies on ejected flames. Suzuki, et al. [40] used several scale models to investigate the effect of balconies on fire spread. In one experiment, a 1/7th scale model was used to represent a seven-story apartment complex. The model was 3.43 m tall by 2.97 m wide by 0.575 m deep as shown in Fig. 2.6(a). The fire room, located 1.03 m from the ground (representing the second floor), was 0.40 m tall by 0.93 m wide by 0.575 m deep. The only opening in the fire room was the 0.27 m tall by 0.60 m wide window (Fig. 2.6(b)). Horizontal balconies extended the entire 2.97 m width for depths of 0, 10, 15, 20 and 25 cm. Three 30 cm square manually controlled propane gas burners, located in the center of the room, provided the fire. The experiment was conducted at four heat release rates: 32, 48, 72, and 95 kW. Arrays of thermocouples were used to measure gas temperatures near the exterior wall, and the fire room temperature was measured by a thermocouple located

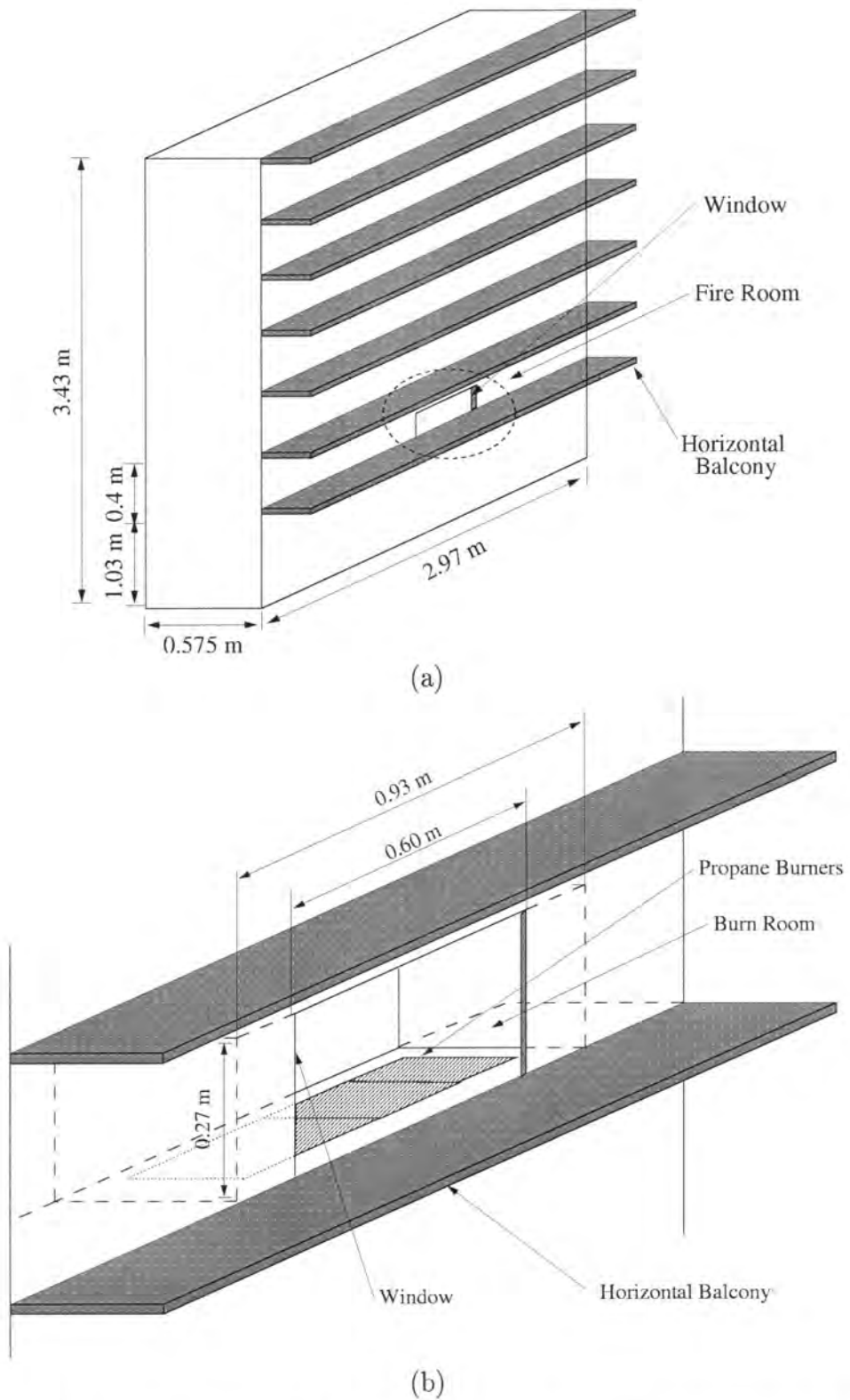


Figure 2.6 (a) Schematic of building geometry and (b) enlargement of fire room geometry for the 1/7 scale experiment for Suzuki et al. [40].

in a corner of the room.

The experiments showed several interesting results. As the balcony depth increased, the burn room temperature increased slightly, which increased the combustion rate and caused the room to flashover more quickly. More importantly, building facade temperature profiles above the fire room illustrated how the balconies projected the flames away from the building facade. Temperatures as low as 70°C were recorded at the floor above the fire floor with a 25 cm balcony. Heat flux measurements at the exterior wall decreased significantly as the balcony depth increased.

A second, more recent experiment by Suzuki, et al. [41] used a 1/3 scale model of a four-story apartment building. As in previous experiments, horizontal balconies spanned the width of the facade but also contained solid balustrades and vertical separation walls (see Fig. 2.7). Again, the tests used three manually controlled propane burners. By determining an “enclosure ratio”, which is the exposed surface area within the balcony itself, Suzuki et al. were able to correlate the effects of balcony depth and geometry to the probability of fire spread. The results showed a high probability of fire spread as the exposed surface area increased based on increased temperature measurements along the exterior wall. While these results show that an infinite balcony depth is most desirable, it is obviously not realistic to implement.

## 2.3 Computational Fire Models

In the past several decades, CFD has undoubtedly benefited from the advances in computational power and decreases in the cost of hardware. Since the 1960’s, computational cost has decreased by a factor of 10 every 8 years, and more so in the last decade [42]. The focus of CFD has changed from developing better numerical models for approximating the governing equations in the 1960’s to solving the governing equations directly (DNS) and improving on the physics of multi-species and reacting flows.

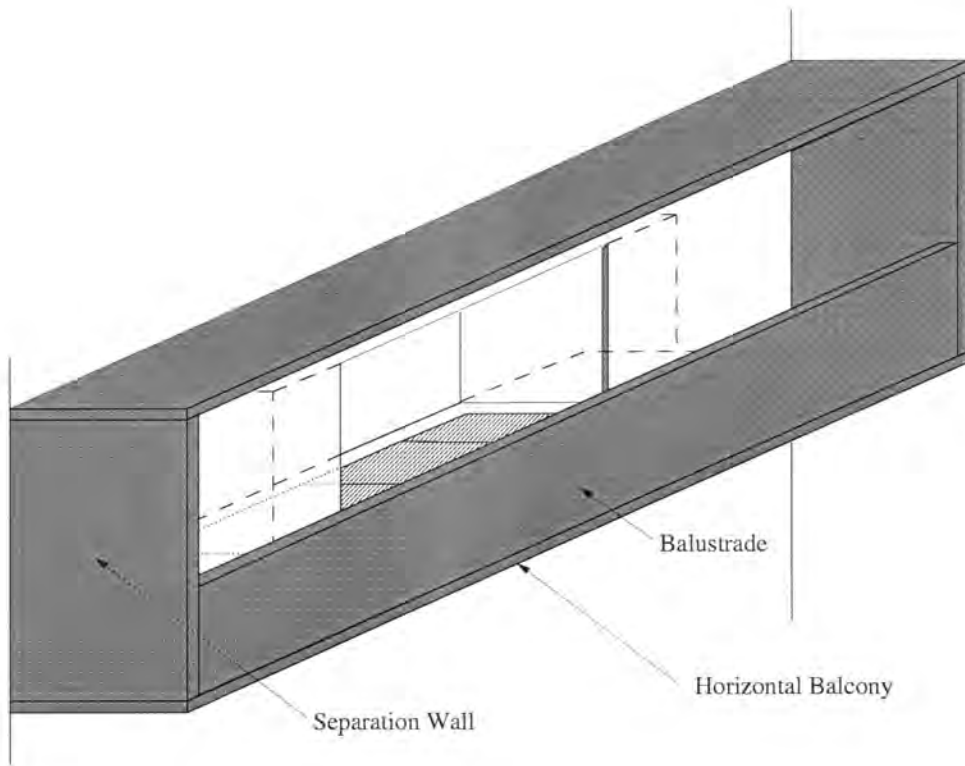


Figure 2.7 Detail of burn room geometry for 1/3 scale model with separation walls and balustrade for Suzuki et al. [41].

Although the governing equations for fluids, heat transfer and combustion were derived over a century ago, according to Hottel, “A case can be made for fire being, next to the life process, the most complex of phenomena to understand” [43]. The difficulty in understanding can be extended to modeling of fire and combustion. The most common CFD models currently used to numerically simulate fire are zone and field models, both of which have inherent problems.

### 2.3.1 Zone Models

Zone models are excellent tools due to their relatively simple formulation and implementation. However, there are underlying assumptions which incur error with zone modeling. For example, zone models assume properties such as temperature can be approximated as constant throughout a zone. Although this approximation holds for

as little as two gas layers [44], it may only apply for simple room/compartment geometries such as depicted in Fig. 1.1. Using more complex compartment geometries can grossly under- or over-estimate zone temperatures. These errors arise from a second major complication with zone models, namely the calculation of pressure and pressure differences.

Small pressure differences across vent openings (e.g. windows or doors) cannot be accurately calculated, as is the case when adjacent room pressures only differ by a small amount. For example, consider two rooms adjoined by a doorway, where the pressure in one room is  $10^5$  Pa (about 1 atm) and the pressure in the adjacent room is  $1.1 \times 10^5$  Pa. The actual pressure difference between the rooms is 0.1 Pa, however, due to computational constraints on how many significant digits are held, the pressure difference between the rooms may be calculated as 0 Pa. Therefore, to have one significant digit in a vent flow calculation, seven digits must be carried for a pressure calculation. Cancellation of digits leads to a loss of significant figures resulting in round-off error and numerical noise. The numerical noise induced by vent flow calculations is amplified when computing other intensive properties such as enthalpy. The calculation of pressure also creates a problem with solving the differential equations.

Differential equations can be stiff if the modeled phenomena have time scales which differ by orders of magnitude. Solutions from solvers which do not account for stiff differential equations will at best be grossly inefficient and at worst give wrong answers [44]. For example, pressure adjusts itself much faster than temperature or smoke layer height. Another problem created by stiff ordinary differential equations (ODE) is the large computational cost even though the solution is changing slowly. Stiff ODE solvers choose a time step size based on stability considerations, while non-stiff solvers choose a step size based on the part of the solution with the shortest time scale. The stiff solver must calculate a nonlinear set of simultaneous equations at each time step, and it is therefore inefficient to use stiff methods for non-stiff problems [44]. Although non-stiff

solvers are typically used in field models, problems still arise.

### 2.3.2 Field Models

As mentioned in Chapter 1, field models are one of the most common CFD compartment fire models. The problems inherent to field models revolve around the competing length and time scales over which combustion occurs. Modeling a small pool fire with a 10–20 cm diameter requires computational resolution of about 1 mm to properly model the physical phenomena occurring, making it computationally costly to model large scale fires such as building, house or forest fires. Numerical methods and models used in field models also create difficulties.

The combustion zone at the base of a fire plume moves due to the quasi-periodic formation of large-scale, low frequency toroidal vortices [45, 46]. While a small pool fire is at best a quasi-steady state process, a compartment or forest fire is truly time dependent and thus makes time averaging approaches such as  $k - \epsilon$  or RANS models inappropriate [47]. If  $k - \epsilon$  or RANS models are used, the results are smoothed, so alternative methods can be used if some idealizations are made to the physics of the combustion and fire plume.

LES along with mixture-fraction based combustion can be used with some simplifications. A LES technique numerically solves the large-scale eddies which govern the mixing of gases. The sub-grid scale motion is idealized by a constant eddy viscosity, whose length scale is tied to the grid resolution and time scale determined by the local resolvable dissipation. However, there is a question of whether the turbulence models compensate for the loss of grid resolution [25], and it is unclear how these parameters affect the solution, or what the solution represents [48]. The loss of resolution certainly affects the importance of the sub-grid radiation and combustion modeling.

The major limitation to the mixture fraction combustion model is that it simplifies the radiative heat transfer and lacks the ability to account for finite rate combustion

reactions. The flame sheet, where combustion occurs, and where radiative feedback is most important cannot be directly simulated, so the radiation is accounted for globally by assuming all locations in the flame lose a fixed amount by radiation [49], discussed later in Chapter 3, Sec. 3.3.

In Chapter 3, the theory for LES-based methodology used in the FDS code will be presented. Discussion of the combustion and radiation models implemented in the code will follow. The numerical formulation of the governing equations and sample temporal and spatial discretizations will be given. Boundary conditions will also be discussed.

## CHAPTER 3 METHODOLOGY

### 3.1 Governing Equations

Large eddy simulation methodology is the basis for the fire dynamics simulator (FDS) code which is used in this research, developed by McGrattan, et al. [22] at the National Institute of Standards and Technology (NIST). The FDS code uses the compressible conservation equations, and allows for multi-species mixtures of ideal gases. Equations 3.1–3.4 are the conservation of mass, species, momentum and energy, respectively

$$\frac{\partial \rho}{\partial t} + \nabla \cdot \rho \mathbf{u} = 0 \quad (3.1)$$

$$\frac{\partial (\rho Y_i)}{\partial t} + \nabla \cdot \rho Y_i \mathbf{u} = \nabla \cdot (\rho D_i) \nabla Y_i + \dot{W}_i''' \quad (3.2)$$

$$\rho \left( \frac{\partial \mathbf{u}}{\partial t} + (\mathbf{u} \cdot \nabla) \mathbf{u} \right) + \nabla p - \rho \mathbf{g} - \mathbf{f} = \nabla \cdot \tau \quad (3.3)$$

$$\frac{\partial (\rho h)}{\partial t} + \nabla \cdot \rho h \mathbf{u} - \frac{Dp}{Dt} = \dot{q}''' + \nabla \cdot k \nabla T + \nabla \cdot \sum_i h_i (\rho D)_i \nabla Y_i \quad (3.4)$$

where the fluid variables are density  $\rho$ , time  $t$ , velocity vector  $\mathbf{u}=(u, v, w)$  for a Cartesian coordinate system  $\mathbf{x}=(x,y,z)$ , mass fraction of  $i$ th species  $Y_i$ , diffusion coefficient  $D_i$ , production rate of  $i$ th species per unit volume  $\dot{W}_i'''$ , gravity vector  $\mathbf{g}$ , external force vector (excluding gravity)  $\mathbf{f}$ , enthalpy  $h$ , pressure  $p$ , heat release rate per unit volume  $\dot{q}'''$ , thermal conductivity  $k$ , and temperature  $T$ . The viscous stress tensor  $\tau$  for a Newtonian fluid is given by

$$\tau_{ij} = \mu \left( \frac{\partial u_i}{\partial x_j} + \frac{\partial u_j}{\partial x_i} - \delta_{ij} \frac{2}{3} \frac{\partial u_k}{\partial x_k} \right) \quad (3.5)$$

The pressure term is decomposed into three components

$$p = p_o - \rho_\infty g z + \tilde{p} \quad (3.6)$$

with background pressure  $p_o$ , hydrostatic pressure  $\rho_\infty g z$  and flow-induced perturbation pressure  $\tilde{p}$ . The temperature and density are inversely proportional in low-Mach number flows [26], so the equation of state can be approximated as

$$p_o = \rho \mathcal{R} T \sum \left( \frac{Y_i}{M_i} \right) = \frac{\rho \mathcal{R} T}{M} \quad (3.7)$$

where  $\mathcal{R}$  is the universal gas constant, and  $M_i$  is molecular weight of the  $i$ th species. The species specific heat  $c_{p,i}$  is assumed to be independent of temperature and pressure. Enthalpy is then approximated as

$$h = \sum_i h_i Y_i = T \sum_i c_{p,i} Y_i \quad (3.8)$$

Each species is assumed to act as a diatomic molecule, so the ratio of specific heats,  $\gamma$ , is taken as 7/5. The equation of state can be restated as

$$p_o = \frac{\gamma - 1}{\gamma} \rho h \quad (3.9)$$

The second term in Eq. 3.1 is decomposed into  $\mathbf{u} \cdot \nabla \rho + \rho \nabla \cdot \mathbf{u}$ . Then using conservation of mass (3.1) and energy (3.4) and taking the material derivative of Eq. 3.9, the divergence of the velocity field  $\nabla \cdot \mathbf{u}$  can be rewritten as

$$\nabla \cdot \mathbf{u} = \frac{\gamma - 1}{\gamma p_o} \left( q''' + \nabla \cdot k \nabla T + \sum_i c_{p,i} T \rho D_i \nabla Y_i - \frac{1}{\gamma - 1} \frac{dp_o}{dt} \right) \quad (3.10)$$

The momentum equation (3.3) can be simplified by subtracting the hydrostatic pressure gradient

$$\frac{\partial \mathbf{u}}{\partial t} + \frac{1}{2} \nabla |\mathbf{u}|^2 - \mathbf{u} \times \boldsymbol{\omega} + \frac{1}{\rho} \nabla \tilde{p} = \frac{1}{\rho} [(\rho - \rho_\infty) \mathbf{g} + \mathbf{f} + \nabla \cdot \boldsymbol{\tau}] \quad (3.11)$$

using the identity  $(\mathbf{u} \cdot \nabla) = \frac{1}{2} \nabla |\mathbf{u}|^2 - \mathbf{u} \times \boldsymbol{\omega}$ . The gradient of pressure head  $\nabla \mathcal{H}$  neglecting potential energy is

$$\nabla \mathcal{H} \approx \frac{1}{2} \nabla |\mathbf{u}|^2 + \frac{1}{\rho} \nabla \tilde{p} \quad (3.12)$$

The previous approximation can be explained by neglecting the baroclinic torque, such that buoyancy is the dominant source of vorticity [22]. Neglecting the baroclinic torque simplifies the elliptic partial differential equation by taking the divergence of the momentum equation

$$\nabla^2 \mathcal{H} = \frac{\partial (\nabla \cdot \mathbf{u})}{\partial t} - \nabla \cdot \mathbf{F} \quad (3.13)$$

$$\mathbf{F} = -\mathbf{u} \times \boldsymbol{\omega} - \frac{1}{\rho} [(\rho - \rho_\infty) \mathbf{g} + \mathbf{f} + \nabla \cdot \boldsymbol{\tau}]$$

Using LES, the grid resolution cannot resolve the turbulent mixing at all scales, so the Smagorinsky sub-grid scale model [50] is used to determine the viscosity

$$\mu = \max(\mu_{\text{DNS}}, \rho(C_s \Delta)^2 |S|) \quad (3.14)$$

$$\mu_{\text{DNS}} = \sum_i Y_i \mu_i$$

where empirical constant  $C_s$ , usually is equal to 0.14 and the filter width  $\Delta$  is on the order of magnitude of a grid cell

$$\Delta = (\delta x \delta y \delta z)^{\frac{1}{3}} \quad (3.15)$$

and  $|S|$  is the magnitude of the deformation tensor

$$|S| = 2 \left( \frac{\partial u}{\partial x} \right)^2 + 2 \left( \frac{\partial v}{\partial y} \right)^2 + 2 \left( \frac{\partial w}{\partial z} \right)^2 + \left( \frac{\partial u}{\partial y} + \frac{\partial v}{\partial x} \right)^2 + \left( \frac{\partial u}{\partial z} + \frac{\partial w}{\partial x} \right)^2 + \left( \frac{\partial v}{\partial z} + \frac{\partial w}{\partial y} \right)^2 \quad (3.16)$$

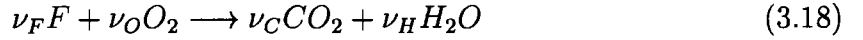
## 3.2 Mixture Fraction Combustion Model

The mixing of fuel and air using LES methodology cannot be directly calculated due to the small length and time scales on which combustion takes place and the large domain over which fires take place. A model developed at the National Institute of Standards and Technology allows for the tracking of the transport of fuel, oxygen and major combustion products using a single conservative scalar quantity, the mixture fraction,  $Z$ , defined as

the fraction of the fluid mass that originates as fuel [47]

$$\begin{aligned} Z &= \frac{sY_F - (Y_O - Y_O^\infty)}{sY_F^I + Y_O^\infty} \\ s &= \frac{\nu_O M_O}{\nu_F M_F} \end{aligned} \quad (3.17)$$

where  $F$  is a hydrocarbon fuel,  $O$  is oxygen,  $Y$  is the mass fraction,  $Y_O^\infty$  is the ambient oxygen mass fraction,  $Y_F^I$  is the fuel mass fraction in the fuel stream and  $\nu$  is the stoichiometric coefficient for the overall one-step combustion reaction



where nitrogen is also present but chemically inactive. The mass fractions of all other species can be derived based on empirical state relationships. The mixture fraction also satisfies the conservation law

$$\rho \frac{DZ}{Dt} = \nabla \cdot \rho D \nabla Z \quad (3.19)$$

The model assumes the reaction of fuel and oxygen takes place infinitely fast, such that fuel and oxidizer cannot co-exist, i.e., they vanish simultaneously.

### 3.3 Radiation Model

The radiative transport equation (RTE) for a non-scattering gray gas is

$$\hat{s} \cdot \nabla I_n(x, \hat{s}) = \kappa_n(x) [I_{b,n}(x) - I(x, \hat{s})], \quad n = 1, \dots, N \quad (3.20)$$

with unit normal direction vector  $\hat{s}$ , radiation intensity  $I$  for band width  $n$ , absorption coefficient  $\kappa$  and blackbody radiation intensity from the Planck function  $I_b$ . To solve the RTE over all wavelengths is computationally expensive, therefore, the radiation spectrum is divided into a small number of bands, and the RTE is derived for each band. In most large-scale fires, soot is the most important combustion product controlling the thermal radiation. The gas can be described as a gray medium, such that the radiation

spectrum of the soot is continuous, reducing the number of spectral bands to a single band ( $N = 1$ ). The absorption coefficients,  $\kappa_n$ , are calculated using a narrow-band model called RADCAL [51], employed by FDS. The absorption coefficient is tabulated as a function of temperature and mixture fraction.

An advantage of the RTE model is improved calculation near the flame sheet, the region within the plume where gaseous fuels combust. Typical grid resolutions are too large to resolve the flame sheet, so temperatures are often under-predicted. The strong dependence of the source term for blackbody radiation,  $k_n I_b$ , on temperature requires a model for grid cells in or near the flame sheet, where

$$\kappa I_b = \begin{cases} \kappa \sigma T^4 / \pi & \text{Outside flame zone} \\ \chi_r q''' / 4\pi & \text{Inside flame zone} \end{cases}$$

where  $\sigma$  is the Stefan-Boltzmann constant and  $\chi_r$  is the radiative fraction loss.

### 3.4 Numerical Formulation

Scalar quantities are defined at the center of each cell, while vector quantities are defined at the cell surfaces, with normals parallel to their respective axis ( $x, y, z$ ) shown in Figure 3.1. The governing equations numerically solved are conservation of mass (3.1), species (3.2), momentum (3.3), the Poisson equation (3.13) and the divergence of the velocity field (3.10). The spatial derivatives are discretized using second-order accurate central differences on a rectilinear grid. The predictor-corrector scheme is used for the convective terms (e.g.,  $\mathbf{u} \cdot \nabla \rho$ ) using upwind-biased and downwind-biased differences respectively. The  $\pm$  symbol means  $+$  in the predictor step and  $-$  in the corrector step, and the opposite notation is for  $\mp$ . A sample discretization for a convective term is

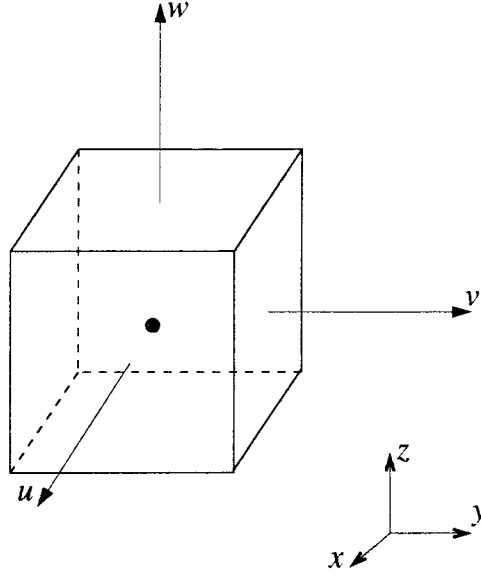


Figure 3.1 Schematic of a computational cell showing velocity vector quantities.

$$\begin{aligned}
 (\mathbf{u} \cdot \nabla \rho)_{ijk} = & \frac{1 \mp \epsilon_u}{2} u_{i,j,k} \frac{\rho_{i+1,j,k} - \rho_{i,j,k}}{\Delta x} + \frac{1 \pm \epsilon_u}{2} u_{i-1,j,k} \frac{\rho_{i,j,k} - \rho_{i-1,j,k}}{\Delta x} + \\
 & \frac{1 \mp \epsilon_v}{2} v_{i,j,k} \frac{\rho_{i,j+1,k} - \rho_{i,j,k}}{\Delta y} + \frac{1 \pm \epsilon_v}{2} v_{i,j-1,k} \frac{\rho_{i,j,k} - \rho_{i,j-1,k}}{\Delta y} + \\
 & \frac{1 \mp \epsilon_w}{2} w_{i,j,k} \frac{\rho_{i,j,k+1} - \rho_{i,j,k}}{\Delta z} + \frac{1 \pm \epsilon_w}{2} w_{i,j,k-1} \frac{\rho_{i,j,k} - \rho_{i,j,k-1}}{\Delta z} \quad (3.21)
 \end{aligned}$$

where  $i, j, k$  are the grid cell indices. The local Courant-Fredrichs-Lewy (CFL) numbers are  $\epsilon_u = u\Delta t/\Delta x$ ,  $\epsilon_v = v\Delta t/\Delta y$ ,  $\epsilon_w = w\Delta t/\Delta z$ . A local CFL number is used to bias the differencing upwind, where

$$\Delta t < \min \left( \frac{\Delta x}{u}, \frac{\Delta y}{v}, \frac{\Delta z}{w} \right) \quad (3.22)$$

If the local CFL number is near unity, the difference becomes nearly fully upwinded, and when the CFL is much less than unity, the differencing is more centralized [42, 52]. A second-order Runge-Kutta scheme advances the velocity and temperature fields. The flow variables are updated in time with an explicit predictor-corrector scheme.

At each time step,  $n$ , the quantities  $\rho^n$ ,  $\mathbf{u}^n$ ,  $Y_i^n$ ,  $\mathcal{H}^n$ , and  $p_o^n$  are known. An example of the temporal discretization of conservation of mass using a second-order explicit

predictor-corrector scheme is given in Eqs. 3.23 and 3.25. The superscript  $n$  is the current time level,  $n + 1$  is the next time level and  $(n + 1)_e$  is an estimated time. The predictor step estimates the variables at the  $(n + 1)_e$  time, where

$$\frac{\rho_{i,j,k}^{(n+1)_e} - \rho_{i,j,k}^n}{\Delta t} + (\mathbf{u} \cdot \nabla \rho)_{i,j,k}^n = -\rho^n (\nabla \cdot \mathbf{u})_{i,j,k}^n \quad (3.23)$$

The Poisson equation for pressure (3.13) is solved using direct fast Fourier transforms solved by the CRAYFISHPAK routine [53]. The velocity is estimated at the next time step, where

$$\mathbf{u}_{i,j,k}^{(n+1)_e} = \mathbf{u}_{i,j,k}^n - \Delta t (\mathbf{F}^n + \nabla \mathcal{H}^n)_{i,j,k} \quad (3.24)$$

Next, the CFL condition is checked for stability, and the time step is reduced if necessary. The dependent variables  $\rho$ ,  $Y_i$  and  $p_o$  are corrected. The corrector step solves for the variables at the  $(n + 1)$  time, where

$$\frac{\rho_{i,j,k}^{(n+1)} - \frac{1}{2} (\rho_{i,j,k}^n + \rho_{i,j,k}^{(n+1)_e})}{\Delta t} + (\mathbf{u} \cdot \nabla \rho)_{i,j,k}^{(n+1)} = \rho_{i,j,k}^{(n+1)_e} (\nabla \cdot \mathbf{u})_{i,j,k}^{(n+1)_e} \quad (3.25)$$

Pressure is then recalculated and velocity corrected. Temperature is calculated from the equation of state (Eq. 3.7). Thermal and material diffusion terms in Eq. 3.10 are central differenced without upwind or downwind bias.

The velocities and pressure are satisfied at a boundary with the relation

$$\frac{\partial \mathcal{H}}{\partial n} = -F_n - \frac{\partial u_n}{\partial t} \quad (3.26)$$

where  $F_n$  is the normal component of  $\mathbf{F}$  at open external boundaries or solid wall. The  $\partial u_n / \partial t$  term is the prescribed rate of change in the normal component of velocity at an opening with a non-zero prescribed pressure. The velocity is initially zero throughout the computational domain. At external boundaries, the pressure head,  $\mathcal{H}$ , is prescribed such that an outgoing flow assumes the pressure perturbation is zero and  $\mathcal{H}$  is constant along streamlines. An incoming flow assumes that  $\mathcal{H}$  is zero infinitely far away, where

$$\mathcal{H} = \frac{|\mathbf{u}|^2}{2} \quad \text{outgoing flow} \quad (3.27)$$

$$\mathcal{H} = 0 \quad \text{incoming flow} \quad (3.28)$$

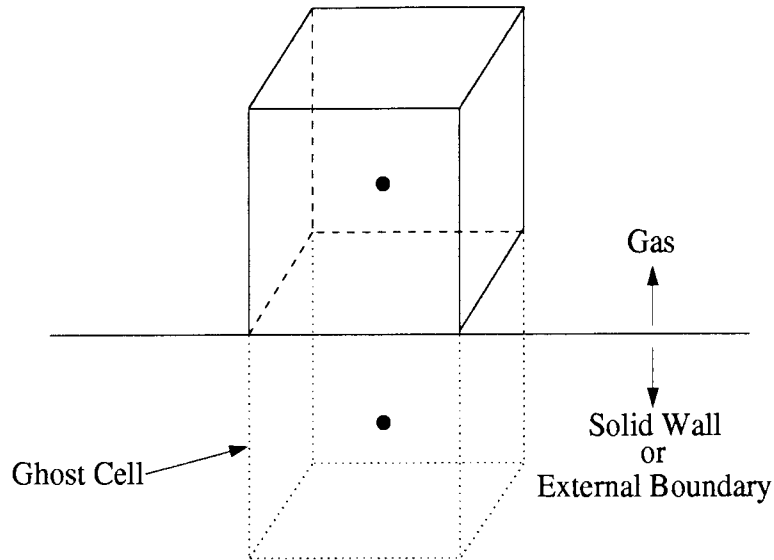


Figure 3.2 Schematic of a wall and ghost cell at a solid wall or boundary.

The scalar quantities  $T$ ,  $Y_i$ ,  $\dot{m}$  and  $\rho$  at a gas/solid interface or external boundary are calculated using a “ghost” cell, depicted in Figure 3.2. When the ghost cell is located within a solid, it does not represent the temperature in the solid, but is used to establish a temperature gradient at a wall. The wall temperature is defined as the temperature at the interface between a ghost and wall cell.

The formulations presented here in Chapter 3 are employed in the FDS code. In the following chapter, combustion validation, building geometry and grid resolution will be discussed. Results will be presented illustrating the effect of balcony depth and geometry on vertical fire spread.

## CHAPTER 4 RESULTS

The focus of this chapter is to present results of how a fire spreads vertically along the exterior of a building when balconies are present. The simulations are conducted using the Fire Dynamics Simulator (FDS) code developed at NIST. The FDS code will be used first to validate the mixture fraction combustion model. Next, the apartment complex geometry will be implemented and a grid resolution study completed. The scaling laws will be discussed to emphasize the need for small scale modeling in fire studies. The effects of balcony depth and geometry is then presented. Finally, preliminary results will be introduced detailing the effect of wind on vertical fire spread.

### 4.1 Combustion Validation

The validity of the mixture fraction combustion model was tested using the McCaffrey correlations [54]. The validation process provides confidence in the LES and combustion model. Baum and McCaffrey [54] define three major zones for a typical fire plume: the continuous (visible) flame near the base of the fire, the intermittent region and plume region. A mathematical correlation was developed from experimental data to determine relationships for centerline temperature and vertical velocity within these three plume regions

$$T = T_{\infty} \left[ 1 + \left( \frac{\kappa}{0.9 (2g)^{0.5}} \right)^2 \left( \frac{z}{\dot{Q}^{2/5}} \right)^{2\eta-1} \right] \quad (4.1)$$

$$w = \kappa \left( \frac{z}{\dot{Q}^{2/5}} \right)^{\eta} \dot{Q}^{1/5} \quad (4.2)$$

Region	Height, $z$ (m)	$\eta$	$\kappa$ ( $m^{1/2}/s$ )
Continuous Flame	$< 0.2425$	$1/2$	6.8
Intermittent	$0.2425-0.6062$	0	1.9
Plume	$>0.6062$	$-1/3$	1.1

Table 4.1 Constants in McCaffrey correlations for a 16 kW propane fire.

where constants  $z$ ,  $\eta$  and  $\kappa$  are given in Table 4.1 for a 16 kW propane fire. Equations 4.1 and 4.2 are the plume centerline temperature  $T$  and centerline vertical velocity  $w$  based on an ambient temperature  $T_\infty$  and heat release rate  $\dot{Q}$  (in kW).

The correlations have been shown to be accurate up to 10 m diameter pool fires. However, the McCaffrey correlations are not accurate near the base of a fire where entrainment occurs. Currently, there is not a consensus among experiments to properly formulate a model near the base. The area surrounding the base of the fire is sensitive to fuel geometry, boundary conditions and experimental apparatus. Experimental measurements near the base are also highly uncertain due to the localized effects such as radiation.

A propane burner was simulated as a pan, with a surface area of  $0.099 \text{ m}^2$ , from which propane gas was continuously emitted and burned yielding a 16 kW fire. The burner size and heat release rate was used from Suzuki et al. [40]. Grid resolutions of  $32 \times 32 \times 64$ ,  $54 \times 54 \times 72$ ,  $64 \times 64 \times 96$  and  $81 \times 81 \times 108$  were tested, and time-averaged centerline temperatures and vertical velocities were used to compare with the McCaffrey correlations.

Figures 4.1 (a) and (b) are time-averaged centerline temperature and vertical velocity profiles, respectively. As seen in Figs. 4.1 (a) and (b), the profiles generally follow the McCaffrey correlations at higher resolutions ( $64 \times 64 \times 96$  and  $81 \times 81 \times 108$ ), therefore dictating the number of cells required for a valid combustion model. In Fig. 4.1 (a) and (b), near the base of the fire, the numerical solutions for temperature and velocity

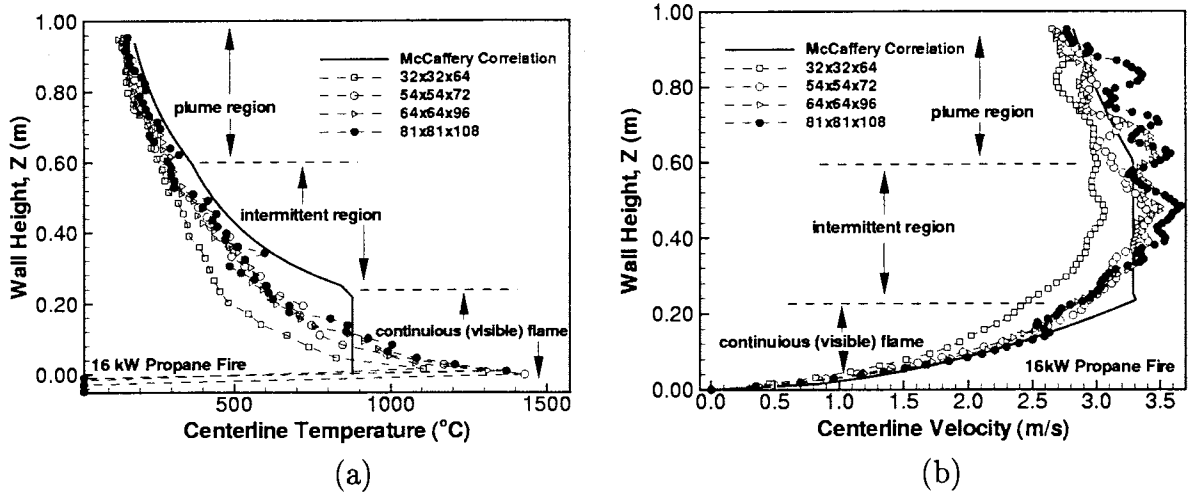


Figure 4.1 Comparison of McCaffrey correlations with LES for the time-averaged centerline (a) temperature and (b) vertical velocity.

deviate from the McCaffrey correlations for reasons mentioned previously.

Based on the results from comparing the simulations to the McCaffrey correlations, the computational grid used for all further simulations is  $81 \times 64 \times 96$  (497,664 cells). Using one 300 MHz processor on an SGI Origin 2200, an average simulation takes approximately  $34 \mu\text{s}$  per time step per cell, and requires 14,350 times steps for 50 seconds of simulation time.

## 4.2 Building Geometry

The building geometry in this research was modeled after the 1/7th scale experiments by Suzuki, et al. [40]. The experimental domain contained a fire floor (located one level above ground floor) and five floors above, each with a balcony of equal depth, as shown in Fig 2.6. Typically, several apartment units are located on each floor and Fig. 4.2 shows three units per floor, however Suzuki et al. [40] only modeled a fire ejecting from a single unit located at the center of the building. The dashed line in Fig. 4.2 illustrates the portion of the building that was numerically simulated in this research. Preliminary

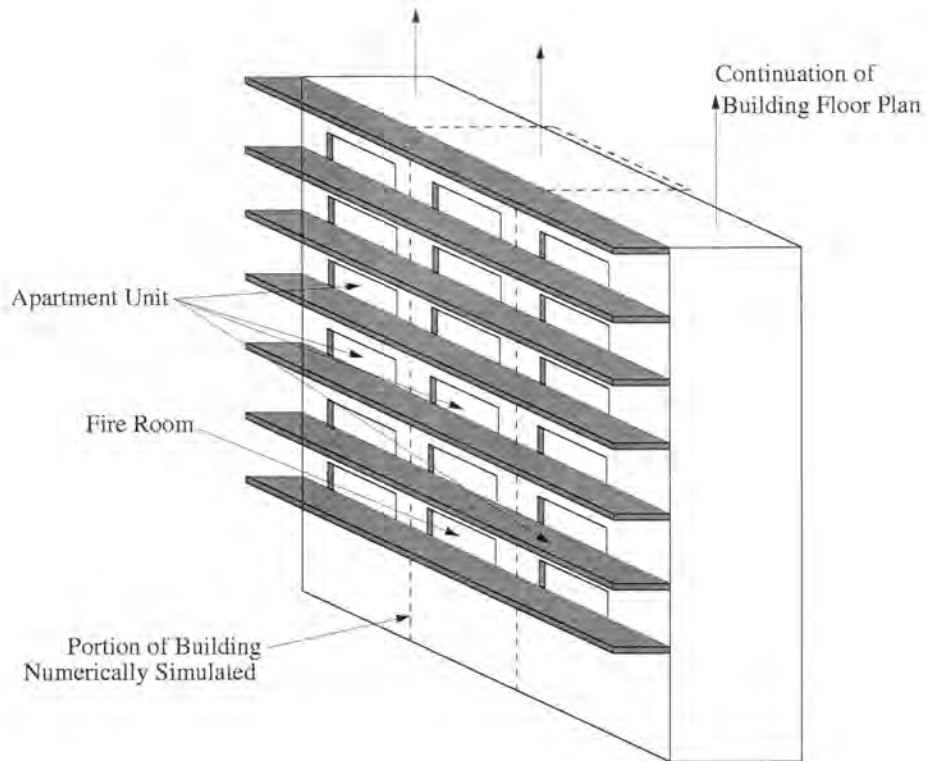


Figure 4.2 Schematic of apartment building, illustrating which portion was numerically simulated.

simulations were performed to determine the minimum number of floors above the fire room that are necessary for a realistic simulation in order to minimize the computational expense. It was determined that simulations of four and five floors were similar to that of a three floor simulation. Therefore, only three floors, the fire floor (FF) and two floors above (FF +1, FF +2), were needed to accurately represent the experiments of Suzuki et al. [40].

Figures 4.3 (a) and (b) show the building geometry for all further numerical simulations. The computational domain has dimensions of  $1220 \times 930 \times 1310 \text{ mm}^3$ , corresponding to  $x, y, z$  directions, respectively. Although the fire room appears to be on the ground floor in the cross-section view (Fig. 4.3 (a)), the floor below the fire room was not included in the numerical simulation, and is accounted for with pressure boundary conditions (refer to Section 4.2.1).

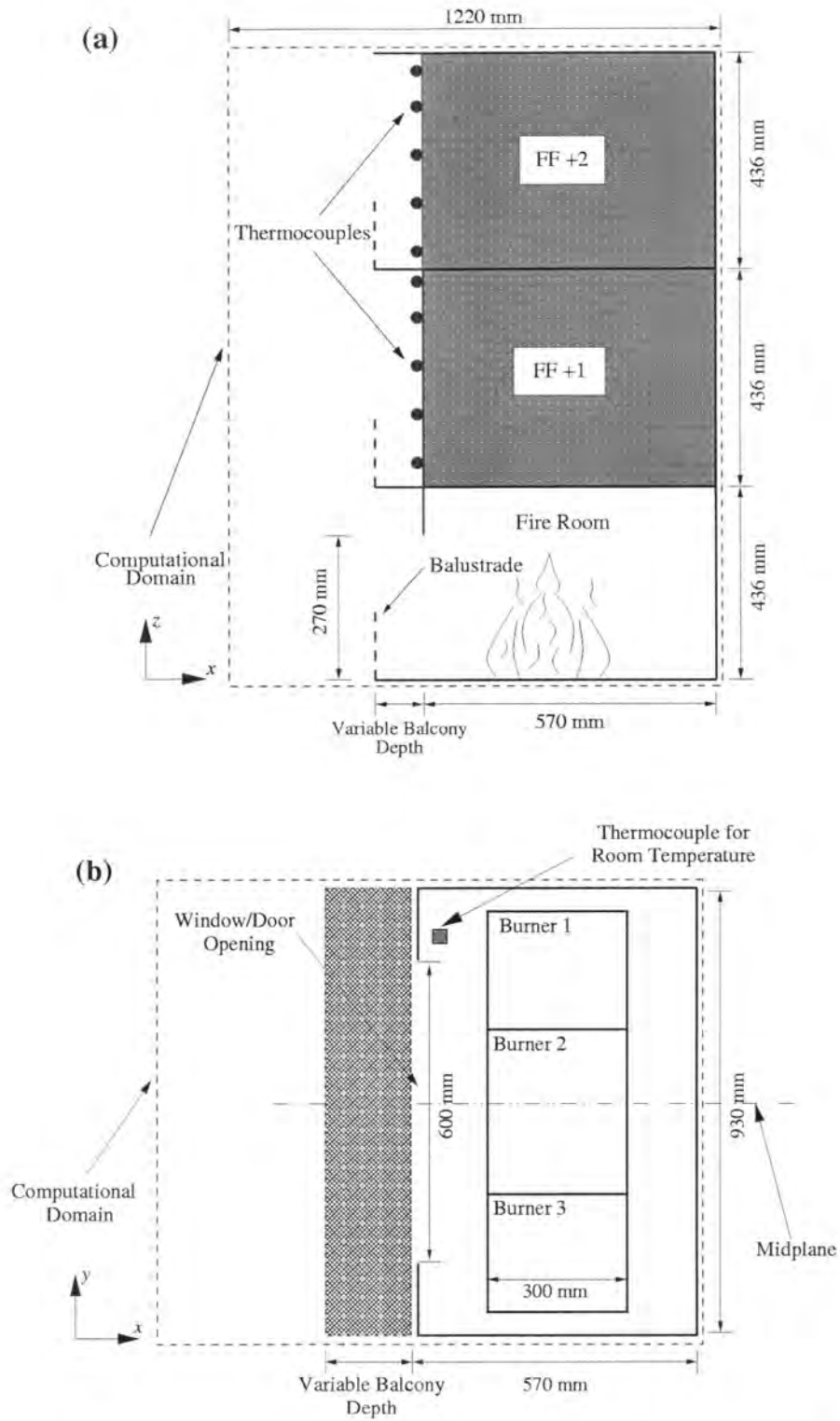


Figure 4.3 Schematic of apartment complex and fire room for (a) cross-section view, and (b) top view.

The window opening can be seen at the fire room, however, FF +1 and FF +2 levels contain no openings, imitating closed windows or doors. For the numerical simulations, five “thermocouples” were equally spaced per floor, located along the exterior walls to record temperature throughout the simulation. In the simulations, the “thermocouple” represents an experimental probe in that the thermocouple is a point in the domain where computational data is extracted. The lowest three thermocouples at both FF +1 and FF +2 are at occupant level, where a person could be standing. More complex balcony geometries may contain balustrades, which are indicated by a vertical dashed line in the cross-section view. The complex geometries will be discussed later in Sec. 4.5. The top view (Fig. 4.3 (b)) shows the three propane burners, each yielding equal heat releases. The balcony extends the entire length of the room (930 mm), while the window opening only extends a portion (600 mm) of the entire width. A thermocouple is also located within the fire room itself, similar to Suzuki et al. [40], to record the fire room temperatures. Although FF +1 and FF +2 were included in the simulations, computation did not occur within FF +1 and FF +2 rooms.

#### 4.2.1 Boundary and Initial Conditions

For the boundary conditions of the computational domain to agree with those of the experiment [40], an “open” boundary is represented at the base of the computational fire floor ( $z=0$ ). This allows the computational domain to treat the bottom boundary as either inflow or outflow external to the building as shown by Eqs. 3.27 and 3.28. As defined by McGrattan, et al. [22], at open external boundaries, a pressure term is prescribed. If the flow is outgoing, the pressure perturbation is zero, and total pressure is constant along streamlines. If the flow is incoming, the total pressure is assumed to be zero infinitely far away. An “inert” thermal boundary condition is specified for all solid surfaces which models an adiabatic surface to eliminate other sources of combustion. Initially the ambient temperature in the computation domain is 21°C, and the velocity

is zero everywhere. After the simulation begins, all temperature and velocity gradients arise from combustion of fuel.

#### 4.2.2 Grid Resolution

Although a grid resolution test was completed previously in Sec. 4.1, the McCaffrey correlations are only used to determine proper grid resolution for combustion. Once the building geometry was specified, a resolution study was completed to determine grid sensitivity of the solutions. The study used four grid resolutions of  $40 \times 32 \times 48$ ,  $60 \times 48 \times 72$ ,  $81 \times 64 \times 96$  and  $90 \times 72 \times 108$  for the geometry depicted in Figures 4.3 (a) and (b) with a 17.5 cm balcony depth (BD) and 48 kW propane fire initiated in the fire room. The exterior wall temperatures at the thermocouples were averaged and used to evaluate grid independence. The thermocouple data was time-averaged over 35 simulation seconds (after the initial transient flow field became quasi-steady) with 700 realizations (data points). As shown in Fig. 4.4, at the floor above the fire floor (FF +1), a course grid generally under-predicts the average exterior wall temperatures, as illustrated by performance of a  $40 \times 32 \times 48$  and  $60 \times 48 \times 72$  grid. The  $81 \times 64 \times 96$  and  $90 \times 72 \times 108$  grids performed similarly at the FF +1, with a maximum error of 8% at the last thermocouple. At FF +2, a course grid generally over-predicts the average wall temperatures and the maximum error between the  $81 \times 64 \times 96$  and  $90 \times 72 \times 108$  grids is 6%. Based on these findings and the CPU requirements, a grid resolution of  $81 \times 64 \times 96$  was chosen and used for further computations.

### 4.3 Scaling Laws

Scaled down experiments and numerical simulations are commonly used as less expensive (monetarily and computationally) alternatives to full scale modeling. However, the scaled down model must accurately represent a full scale fire scenario. In order to

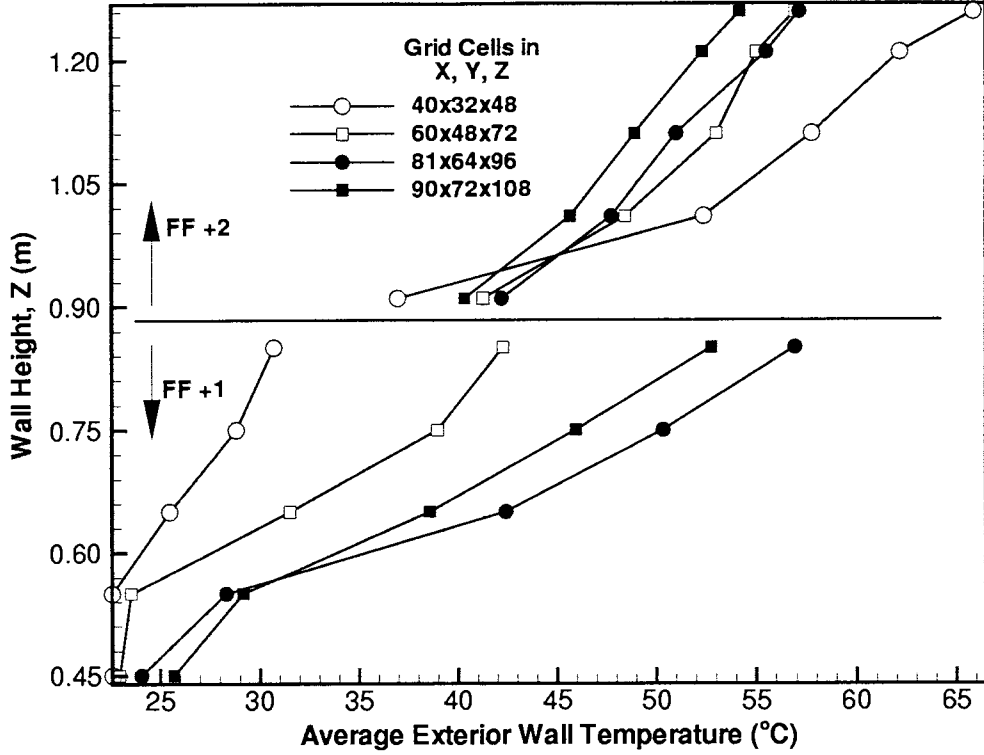


Figure 4.4 Average exterior wall temperatures versus wall height for a 48 kW propane fire and 17.5 cm BD for grid resolution study.

ensure that a scale model exhibits the same behavior as the full scale model, a mathematical correlation must exist between primitive variables. Scaling laws for fires were developed by Byram [15] using  $\pi$ -term techniques for heat release rates

$$\frac{L_m}{L_f} = \frac{D_{h,m}}{D_{h,f}} = \left[ \frac{(\dot{Q})_m}{(\dot{Q})_f} \right]^{\frac{2}{5}} \quad (4.3)$$

where  $m$  denotes model,  $f$  denotes full scale,  $L$  is the length of the flame,  $D_h$  is the hydraulic diameter at the base of the fire, and  $\dot{Q}$  is the total heat release rate.

The ratio in Eq. 4.3 represents the relationship between scaled down and full scale modeling. For the numerical simulations previously discussed,  $L_m/L_f=1/7$  and the model heat outputs based on the experiments are known (48, 72, 95 kW) [40]. Table 4.2 summarizes the relationship for heat release rate using Eq. 4.3. The full heat release rates are typical of actual full scale building fires. A similar size occupant dwelling with

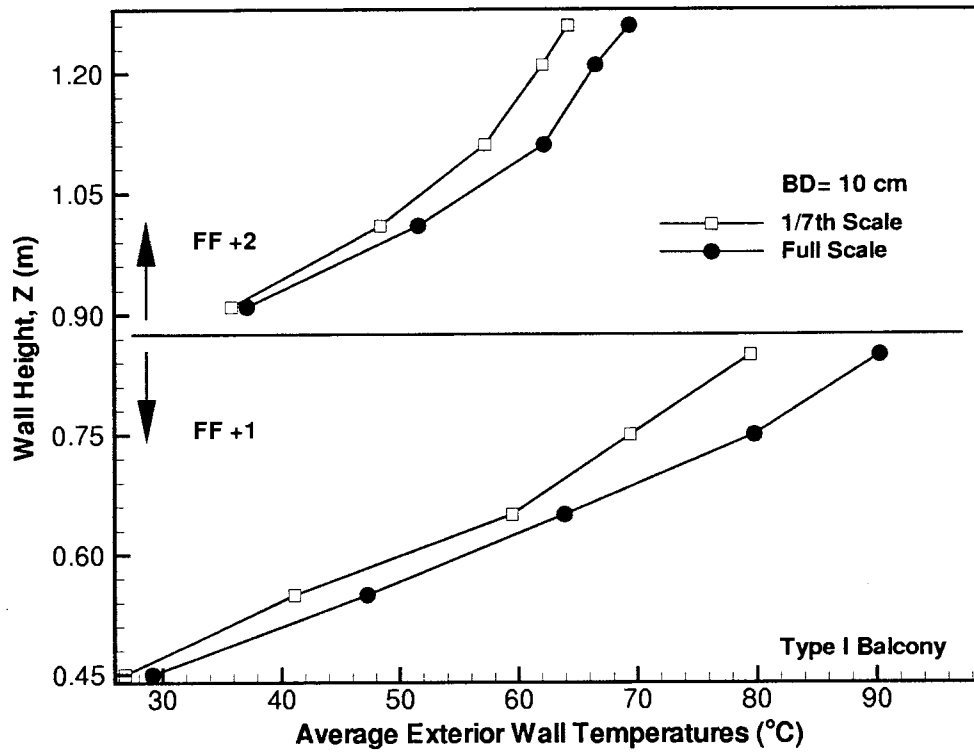


Figure 4.5 Average exterior wall temperatures versus wall height comparing a full scale 6.22 MW fire versus 1/7th scale 48 kW fire.

typical commodities will generate anywhere between 3–10 MW for a fully developed fire [28], however, the 12.3 MW (95 kW model scale) fire is unrealistic for this size apartment complex. Comparing full scale to 1/7th scale, one would expect to observe similar temperature contours and exterior wall temperatures. Figure 4.5 compares the time-averaged temperatures at the exterior wall for the 1/7th scaled fire model (48 kW) and the full scale fire (6.22 MW) for a 10 cm balcony depth (0.7 m for full scale). The

Scale	Model Heat Release	Full Heat Release
1/7	48 kW	6.22 MW
1/7	72 kW	9.33 MW
1/7	95 kW	12.3 MW

Table 4.2 Comparison of model to full scale heat release rates.

overall trends between the model and full scale simulations indicate good agreement, thus validating that the 48 kW 1/7th scale fire is representative of a 6.22 MW fire at full scale. Therefore, the 1/7th model scale will be used for all further simulations herein.

#### 4.4 Effect of Balcony Depth

Gas temperatures are averaged at the midplane for each thermocouple and are shown as contour plots in Figs. 4.6 (a)–(e). Each frame in Fig. 4.6 represents a different balcony depth from 0 – 20 cm (0 – 1.4 m full scale). As the balcony depth increases (frames (a) to (e)), the average temperature at the window of the fire floor increases from 300°C to 400°C, suggesting that room temperature increases as well, supporting the findings by Suzuki et al. [40]. At the first floor above the fire floor (FF +1) for BD=10 cm, the 70°C contour starts at the edge of the balcony and reaches about midway above the balcony at occupant level. As the balcony depth increases (frame (c)), the 70°C regime projects away from the facade. At a balcony depth of 17.5 cm (frame (d)), the 70°C contour has almost completely moved away from FF +1 and FF +2 walls. In fact, balcony temperatures as low as 30°C are seen for a balcony depth of 20 cm (frame (e)) at both FF +1 and FF +2. It is evident that the balcony deflects the movement of hot gases away from the exterior facade of the building as the balcony depth increases.

The numerical simulations shown in Fig. 4.6 have the same general trends as the experiments by Suzuki et al. [40] for a 48 kW propane fire. Suzuki et al. used a grid of thermocouples located at the midplane of the building to record enough data to construct isotherm lines. There are some subtle differences evident in the temperatures from the simulation compared to that of experiments. For example, in the experiments for a 15 cm BD, the temperatures midway between the FF +1 and FF +2 range from 100–200°C, while temperatures in the computational simulations range from 50–135°C. Similar trends occur at all other balcony depths. These differences in temperature are

attributed to the adiabatic boundary condition imposed at all surfaces in contrast to the real behavior of the experimental surfaces. The total heat release rate from the experimental propane burners was about 48 kW, but the burning of building materials in the experiment may have contributed to the overall heat release, especially radiation heat transfer. In the numerical simulations with “inert” materials, there are no additional contributions to the overall heat release rate. The numerical simulations also neglect heat exchange between the fire and surrounding walls, thus all radiation emanating from the compartment is directly from the fire and hot gases. The walls in the experiment [40] received heat from the fire, and thus became a secondary emitter of radiation, along with the fire itself. The radiation feedback model in the numerical simulations only accounts for some of the feedback, near the base of the flame. These differences are also found with the fire room temperatures. The experimental fire room temperatures were about 90°–150°C higher than in the numerical simulations.

The temperatures along the external wall greatly illustrate the effect of the balcony. Figure 4.7 shows a plot of the time averaged external wall temperatures. The lower frame is for temperatures immediately above the fire floor (FF +1) and the upper frame is two floors above (FF +2). As the balcony depth increases from 0–20 cm, the wall temperatures decrease significantly at both FF +1 and FF +2. The curve for BD=0.0 cm indicates that as the fire spreads upward from FF +1 to FF +2, there is a gradual decrease in temperature along the surface. However, once a balcony is in place, there is a distinct discontinuity in the curves from one floor to the next, and the temperatures are significantly lower along the upper surfaces compared to no balcony. The temperatures at the lowest thermocouple ( $z=0.45$  m) decrease slightly as the BD increases from 10 to 17.5 cm, and the temperature gradient for BD=20 cm is the smallest. The results suggest that a balcony depth greater than 15 cm greatly reduces the temperatures along FF +1 and FF +2 as compared to the other balcony depths in this study. The reduction in temperature not only reduces vertical fire spread, but also increases the probability

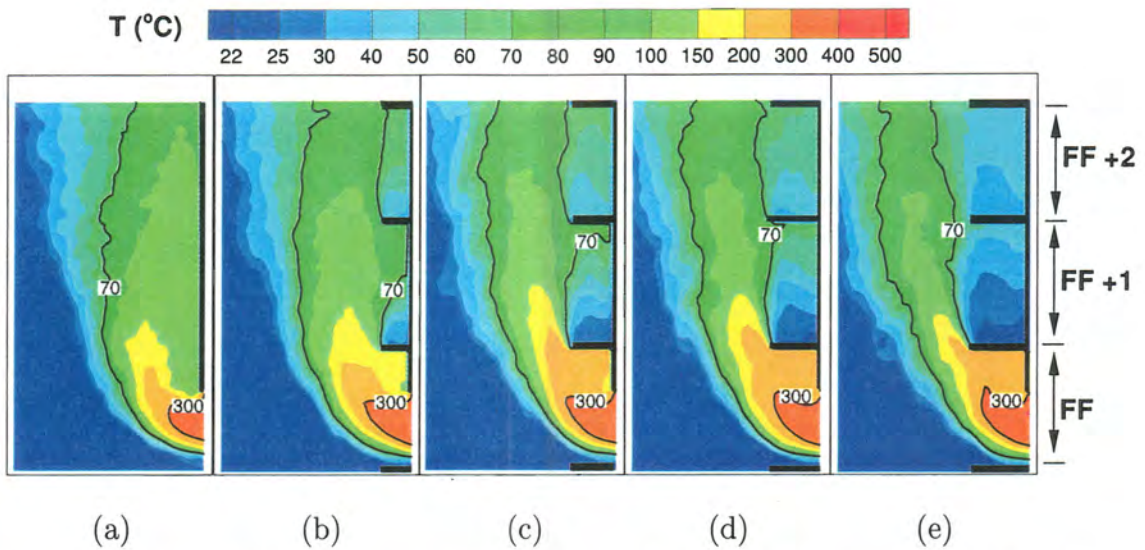


Figure 4.6 Average temperature contours for a 48 kW propane fire for balcony depths of (a) 0 cm, (b) 10 cm, (c) 15 cm, (d) 17.5 cm and (e) 20 cm.

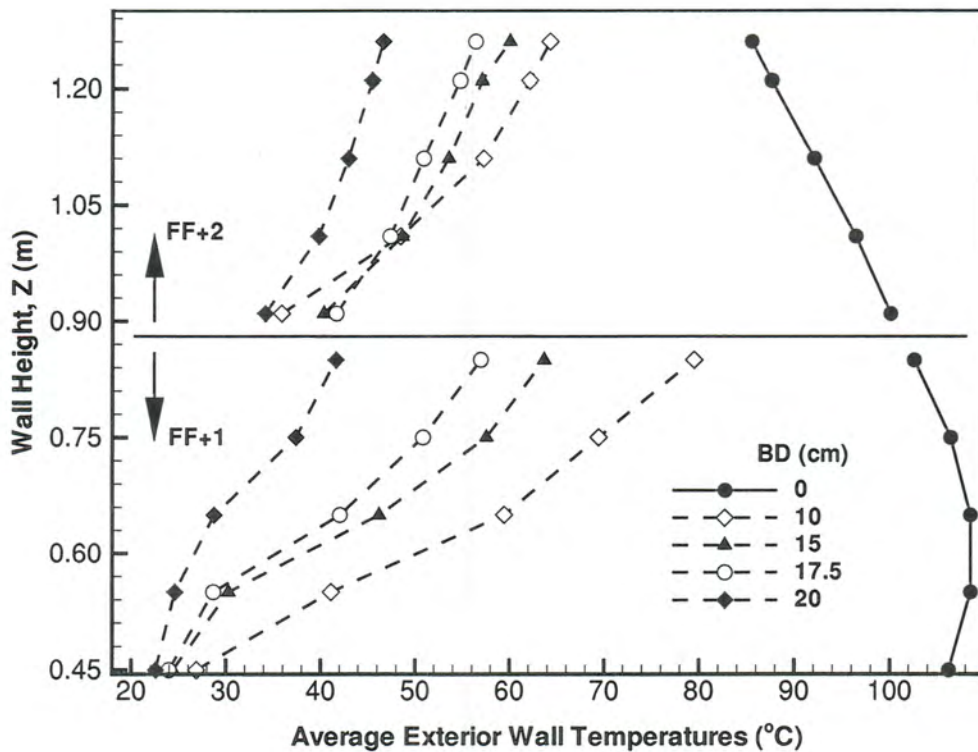


Figure 4.7 Average exterior wall temperatures versus wall height for a 48 kW propane fire.

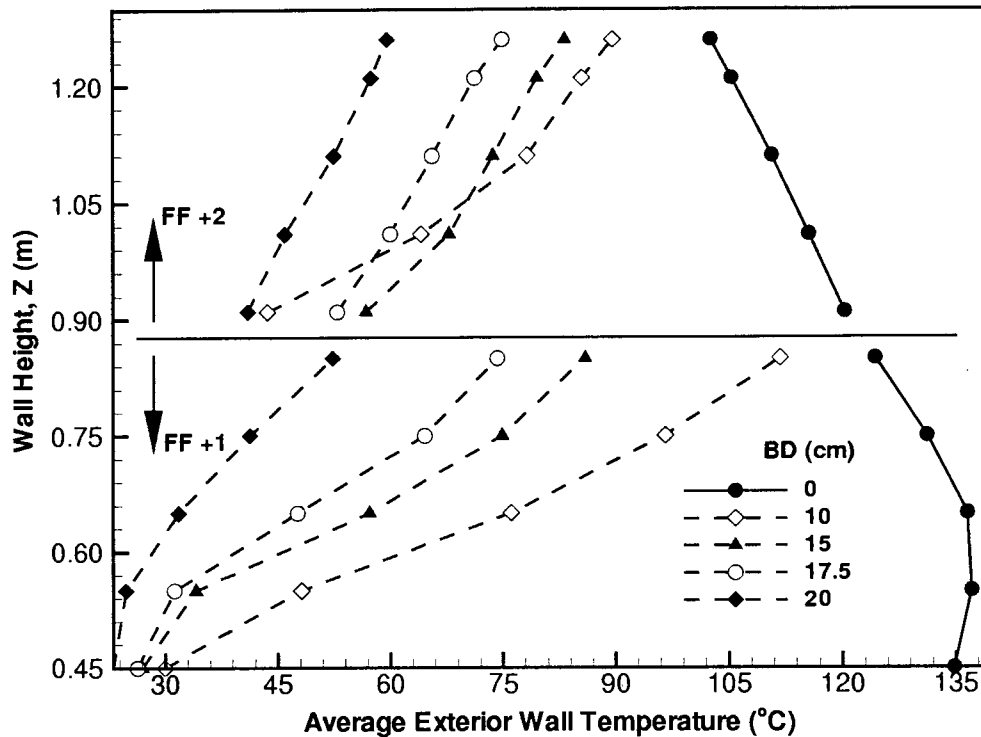


Figure 4.8 Average exterior wall temperatures versus wall height for a 95 kW propane fire.

of human survival on floors directly above the fire floor.

Numerical simulations were completed to investigate the effects of balcony depth with heat release. Balcony depths of 0, 10, 15, 17.5 and 20 cm were simulated using a propane burner yielding a 95 kW heat release, keeping all other variables unchanged. Figure 4.8 shows a plot of the time averaged external wall temperatures. Similar to Fig. 4.7, the lower frame is for temperatures immediately above the fire floor (FF +1) and the upper frame is two floors above (FF +2). The temperature curves for the 95 kW fire (Fig. 4.8) are similar to that of the 48 kW fire (Fig. 4.7), although the temperatures are slightly higher for the larger fire (95 kW), as expected.

## 4.5 Effect of Balcony Geometry

Balcony geometries were examined based on common construction types around the U.S. and internationally. The presence of a solid balustrade and/or separation walls will greatly affect the performance of the balcony. The balustrades are vertical balusters topped by a rail located at the edge of the balcony to keep occupants from falling off the balcony. Examples of balconies are shown in Figure 4.9. Balustrades can either be open with thin metal balusters (Figs. 4.9 (a) and (d)) or solid (Figs. 4.9 (b) and (c)). If a separation wall is present, it extends vertically from one balcony to another (Figs. 4.9 (b) and (d)). Separation walls are typically used for privacy between balconies on the same floor.

### 4.5.1 Boundary Conditions for Balustrades

To evaluate the presence of more complex balcony geometries on vertical fire spread, several different balcony types were identified and defined, as listed in Table 4.3 corresponding to Fig. 4.9 (a)–(d). The geometry is represented in Fig. 4.3 (a) and (b), and the balustrade (dashed line in Fig. 4.3 (a)) is now implemented. Balustrades consisting of non-combustible rails (Fig. 4.9 (a)) and partial separation walls (Fig. 4.9 (c)) do not greatly disrupt the upward flow of gases, and thus were left out of the numerical model (listed as open in Table 4.3). If the balustrade contains thick rails (Fig. 4.9 (b)) or complete separation walls (Fig. 4.9 (d)), the upward gas flow is affected, and thus included in the numerical model (listed as solid in Table 4.3). The balcony geometry discussed previously in Sec. 4.4 is considered a Type I balcony.

Each balcony type, shown in Fig. 4.9 (a)–(d), is constructed of non-combustible materials, and modeled as such in the numerical simulations. Types I and III are similar in construction in that the balcony protrudes from the building. However, Type III has a solid (brick) balustrade whereas Type I has an open (metal) balustrade. Balcony



(a)

(b)



(c)

(d)

Figure 4.9 Balcony Configurations: (a) Type I, (b) Type II, (c) Type III, (d) Type IV (Photos by author).

Type	Building Material	Balustrade	Separation Wall	Fig. 4.9
I	Steel	Open	Open	(a)
II	Concrete/Brick	Solid	Solid	(b)
III	Steel/Brick	Solid	Open	(c)
IV	Steel/Concrete	Open	Solid	(d)

Table 4.3 Definitions for various complex balcony geometries.

Types II and IV pose a more difficult problem, due to the fact that the balconies are within a partial enclosure of the building itself. Type II is considered fully enclosed (solid balustrade and separation wall). The overall concern and focus of this study is to determine which balcony geometry provides the most protection against vertical fire spread and human survivability at floors above a fire floor.

#### 4.5.2 Comparison of Balcony Types

The newest research by Suzuki et al. [41] suggests that as the enclosure ratio increases, the balcony becomes less effective. The enclosure ratio, as defined by Suzuki et al., is the surface area enclosed within the balcony itself. As shown in Table 4.3, the Type II balcony would have the largest enclosure ratio of all the types tested in the numerical calculations.

The effect of the balcony geometry is illustrated in Figs. 4.10 (a)–(d). The time averaged temperature contours are shown for balcony Types I–IV, holding the balcony depth constant at 17.5 cm. Although the building geometry in Figs. 4.10 (a) and (d), Types I and IV respectively, look similar, Fig. 4.10 (d) includes solid separation walls parallel to the plane of the figure. Figures 4.10 (b) and (c), Types II and III respectively, also look geometrically similar, however Fig. 4.10 (b) includes solid separation walls parallel to the plane of the figure and the Type III balcony does not.

The average temperature at the window of the FF for a Type I balcony (Fig. 4.10

(a)) is clearly lower than that of Types II and III, and similar to that of a Type IV balcony suggesting increased fire room temperatures for balcony Types II and III. The solid balustrade restricts the flow of hot gases issuing from the fire room and entrains ambient fluid which contributes toward more complete mixing in the room, increasing combustion. The Type I balcony shows the plume of smoke and flame projecting away from the exterior wall. Temperatures between 25–50°C and 30–60°C are seen at the occupant height at FF +1 and FF +2 respectively. For Types II and III (Figs. 4.10 (b) and (c)), the smoke attaches itself to the solid balustrade. The attachment phenomenon can be explained by the Coanda effect. Coanda found that a fluid moving parallel to a stationary surface tends to attach to that surface [55]. When the fluid stream attaches to a surface, it is accompanied by an increase in velocity and decrease in pressure. Thus, the smoke and flames are not projected away from the exterior wall, but are entrained and partially trapped at the FF +1 and FF +2 levels. Temperatures as high as 100°C are located at occupant level for FF +1.

Balcony Type IV (Fig 4.10 (d)), with a solid separation wall, shows similar gas temperatures as Types II and III, but the gas plume is projected further away from the facade similar to Type I. Due to the geometry of Type IV, the smoke most probably attaches itself to the separation wall, which then directs the smoke and heat upward, similar to a chimney. This theory is supported by Oleszkiewicz's [37] research, in which he showed that vertical projections placed alongside a window directed the hot gas upward.

Based on the movement of hot gases, as shown in Figs. 4.10 (a)–(d), the Type I balcony is clearly the most effective at reducing temperatures at floors above the fire floor. These results are further represented in Fig. 4.11; the exterior wall temperatures at FF +1 and FF +2 for the Type I balcony are considerably lower than that of all other types. Types II–IV seem to offer very little protection from heat, especially at the FF +2 level. The higher temperatures increase the possibility of vertical fire spread,

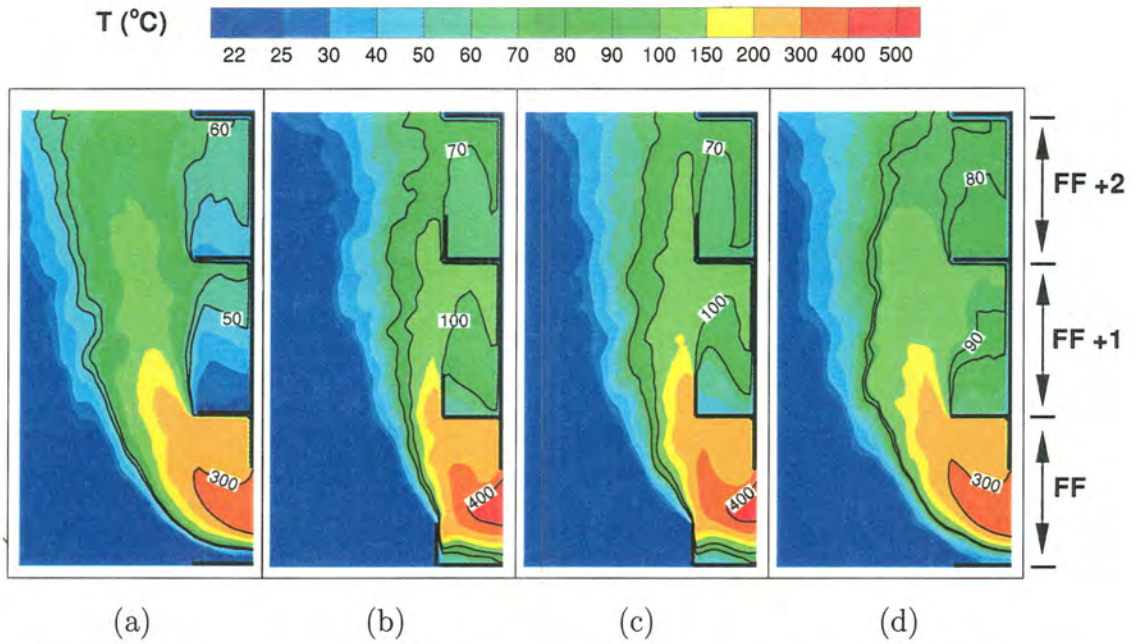


Figure 4.10 Average temperature contours for a 48 kW propane fire for balcony Types (a) I, (b) II), (c) III and (d) IV with  $BD=17.5$  cm.

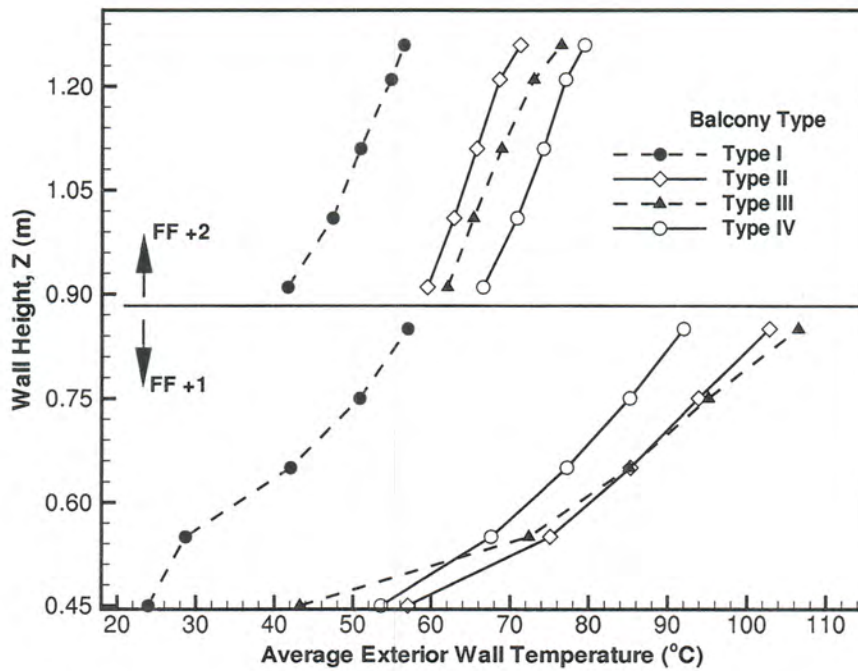


Figure 4.11 Average exterior wall temperatures versus wall height for a 48 kW propane fire for Types I–IV balconies.

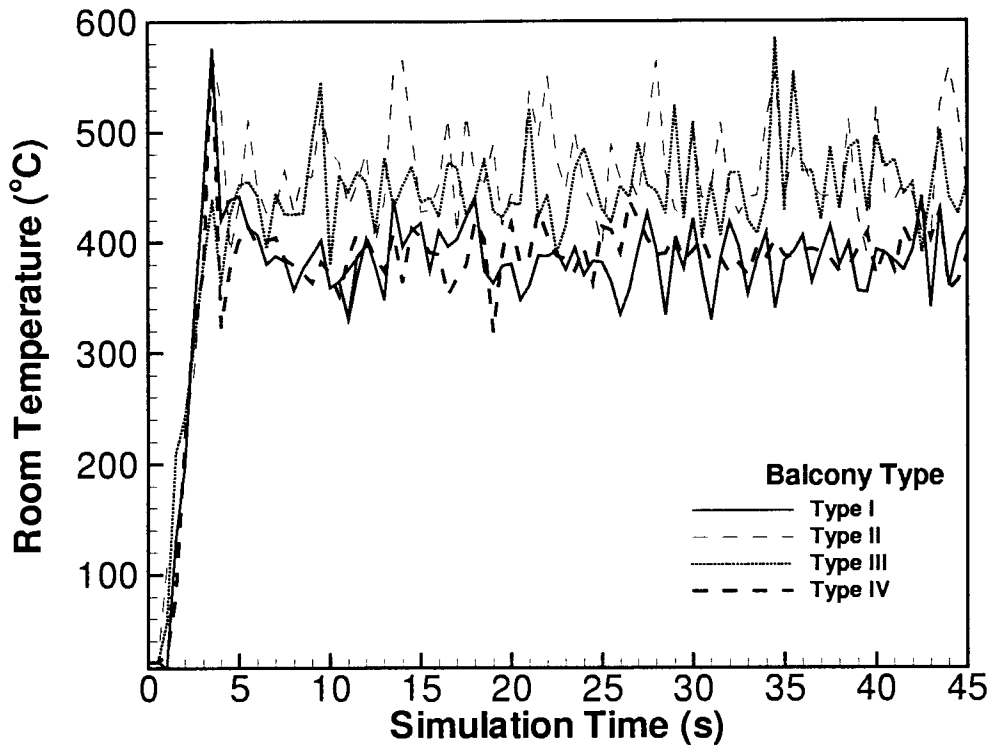


Figure 4.12 Instantaneous room temperature for a 48 kW propane fire for Types I–IV balconies with a 17.5 cm BD.

as well as decrease the possibility that people above the fire floor could survive if trapped on a balcony.

The findings are further demonstrated in Fig. 4.12. The figure shows the instantaneous room temperature for the entire length of a simulation. The room temperature for Types II and III are about 50°C higher than that of Types I and IV. As the amount of surface area outside the fire room increases (i.e. as the enclosure ratio increases), the fire room temperatures increase. It is expected that the radiant heat emitted during a fire for balcony Types II and III will be much larger than for Types I and IV.

## 4.6 Wind Effects

All previous simulations presented were completed without wind impinging on the high rise building, which does not properly represent the environment in which buildings exist. The effect of wind on high rise buildings has been studied computationally [56] and experimentally [57]. However, the effect of wind impinging on high rise buildings with balconies has not been investigated. A preliminary study was conducted to determine such effects.

### 4.6.1 Building Geometry

Using the same building geometry presented in Sec. 4.2, the computational boundary was extended in the  $x$ -direction to allow for wind to develop prior to impinging the front of the building (see Fig. 4.13). The window opening, burner size and fire room dimensions remain the same. A 17.5 cm balcony depth and Type I balcony was used for all simulations which included wind at various angles  $\theta$ .

### 4.6.2 Boundary and Initial Conditions

The boundary and initial conditions for simulations including wind were similar to that previously stated in Sec. 4.2.1. However, wind was simulated by specifying a velocity vector at the  $x - z$  and  $y - z$  boundary. Simulations were completed for wind angles of  $\theta = 0^\circ, 10^\circ, 30^\circ$  and  $45^\circ$ , where  $0^\circ$  is parallel and  $90^\circ$  is normal to the facade of the building.

### 4.6.3 Scaling Laws for Wind

The wind velocity must be scaled properly to correspond with wind at full scale. Wind scaling laws experimentally tested by Emori and Saito [58] were used by Naruse

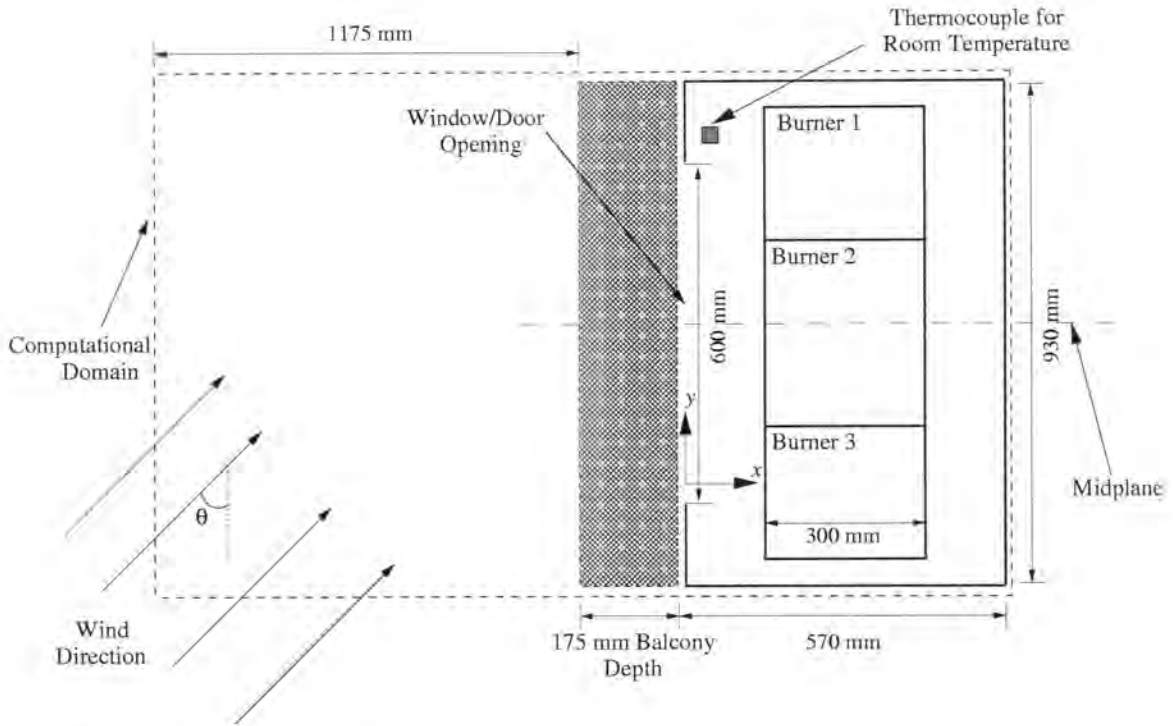


Figure 4.13 Schematic of a top view of an apartment complex and fire room for  $\theta = 45^\circ$  wind simulations.

and Hasemi [57]

$$\frac{V_f}{V_m} = \left( \frac{L_f}{L_m} \right)^{\frac{1}{2}} \quad (4.4)$$

where  $m$  denotes model,  $f$  denotes full scale,  $V$  is the wind velocity and  $L$  is the length of the flame. The ratio in Eq. 4.4 represents the relationship between full scale and scaled down modeling. As previously discussed in Sec. 4.3,  $L_f/L_m=7$ . Table 4.4 summarizes the relationship for wind velocities using Eq. 4.4. A full scale wind velocity of 4.1 m/s was chosen, corresponding to a model velocity of 1.5 m/s for the 1/7th scale for all further simulations.

#### 4.6.4 Wind Impinging on a High Rise Building with Balconies

Instantaneous temperature contours with wind angle  $\theta = 45^\circ$  are shown in Figs. 4.14 (a)–(f) at various  $y$ -positions when  $t=48$  seconds. Frame (a), when  $y=0.48$  m, is just

Scale	Full Scale Velocity	Model Scale Velocity
7/1	0.45 m/s	0.17 m/s
7/1	2.24 m/s	0.85 m/s
7/1	4.10 m/s	1.50 m/s

Table 4.4 Comparison of full to model scale wind velocities.

beyond the midplane at which thermocouples are located at FF +1 and FF +2 (the same plane shown in Fig. 4.3). Frames (b)–(f) are  $y$ –planes moving downwind from the midplane ending with frame (f) at the computational boundary ( $y=0.93$  m).

In frame (a), the hot gas plume does not rise vertically as was shown in previous simulations without wind, and temperatures at FF +1 and FF +2 have not risen above ambient. Further downwind, frame (c) shows that the hot gas is attaching to the underside of the FF +1 balcony. The attachment can be seen continuing through frames (d) and (f). At  $y=0.93$  m (frame (f)), the formation of a torus-like shape plume begins, suggesting that hot gas is rotating beneath the FF +1 balcony and may continue to do so along the entire width of the building. A view of the building in the  $y - Z$  plane will lend insight into what maybe be occurring with the hot gas plume.

Figures 4.15 (a)–(f) show the instantaneous temperature contours at the facade of the building with wind angle  $\theta = 45^\circ$  at various  $x$ -positions when  $t=48$  seconds. The window opening can be seen, and balconies at FF, FF +1 and FF +2 are seen as horizontal lines. Frame (a) is physically located at the facade of the building ( $x = -0.015$  m), while each progressive frame (b)–(e) moves outward from the facade toward the edge of the balcony, frame (f) ( $x = -0.180$  m).

Similarly, Figs. 4.15 (a)–(f) show that temperatures at FF +1 and FF +2 have not risen above ambient. Frame (a) in Fig. 4.15 shows the ejecting hot gas is not symmetric about the window, which is expected because of wind impinging from the right side of the domain. Moving outward from the facade in frames (b)–(e), the hot gas is trapped

below the FF +1 balcony where temperatures as high as  $400^{\circ}$ – $500^{\circ}\text{C}$  can be seen. Only at the end of the balcony (frame (f)) have temperatures above the FF +1 balcony risen above ambient ( $21^{\circ}\text{C}$ ). The trapped hot gas, moving along the underside of the FF +1 balcony now presents a horizontal fire spread hazard, rather than vertical.

Simulations with wind at angles of  $0^{\circ}$ ,  $10^{\circ}$ ,  $30^{\circ}$  also show similar trends to that of wind at  $45^{\circ}$ . As the direction of wind becomes parallel with facade of the building ( $\theta = 0^{\circ}$ ), the hot gas is carried further along the underside of the FF +1 balcony, however, the rotation of gas seen in Fig. 4.14 (f) is not apparent. Temperatures in a range of  $300^{\circ}$  –  $500^{\circ}\text{C}$  are present below the FF +1 balcony. The effect of wind clearly changes the dynamics of the gas plume from that of a buoyant plume creating a vertical fire spread hazard to that of wind driven fires, which are more hazardous in the horizontal (downwind) direction.

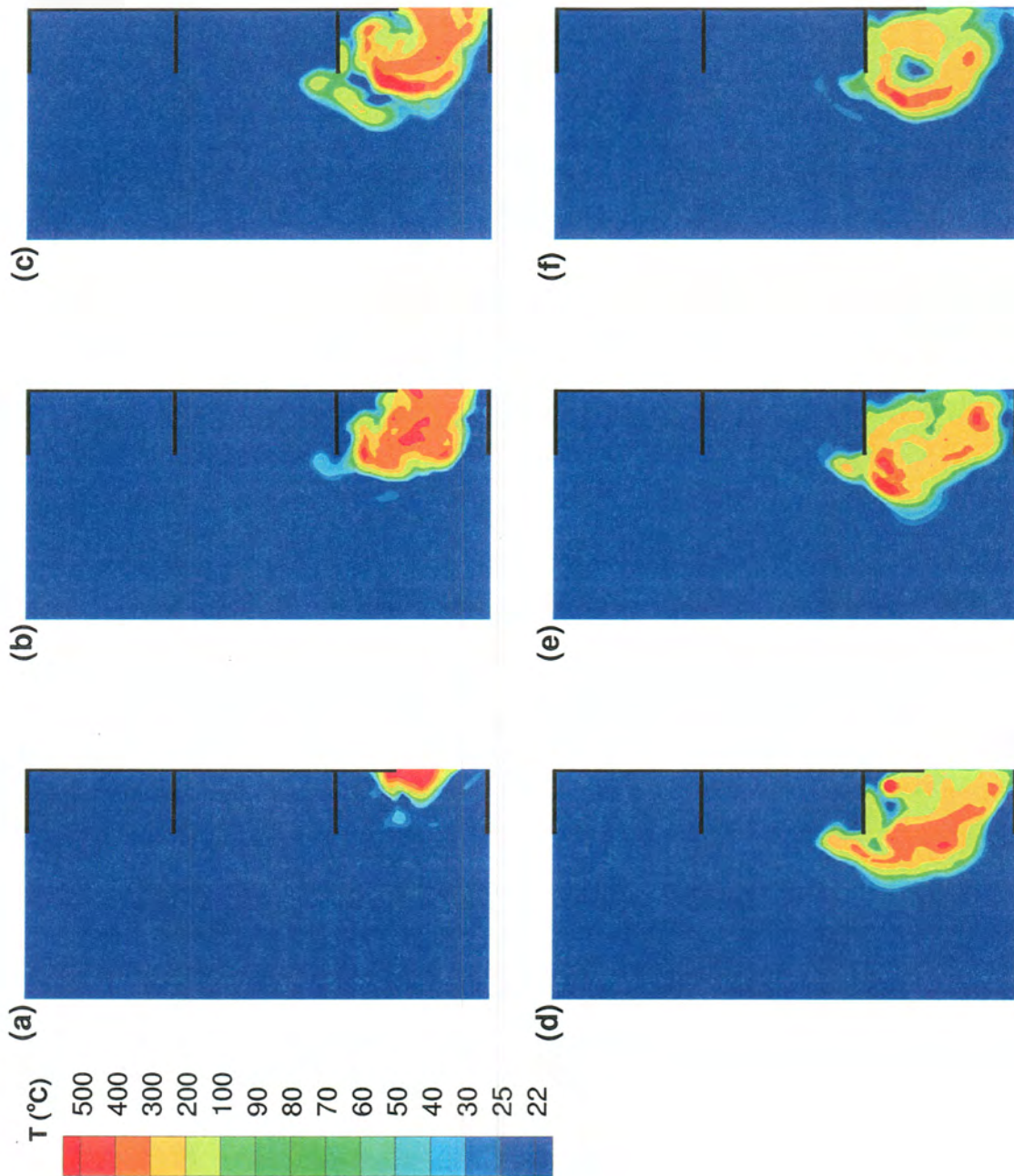


Figure 4.14 Instantaneous temperature contours at  $t=48$  s and wind angle  $\theta=45^\circ$  at locations (a)  $y=0.48$  m, (b)  $y=0.71$  m, (c)  $y=0.77$  m, (d)  $y=0.83$  m, (e)  $y=0.89$  m and (f)  $y=0.93$  m.

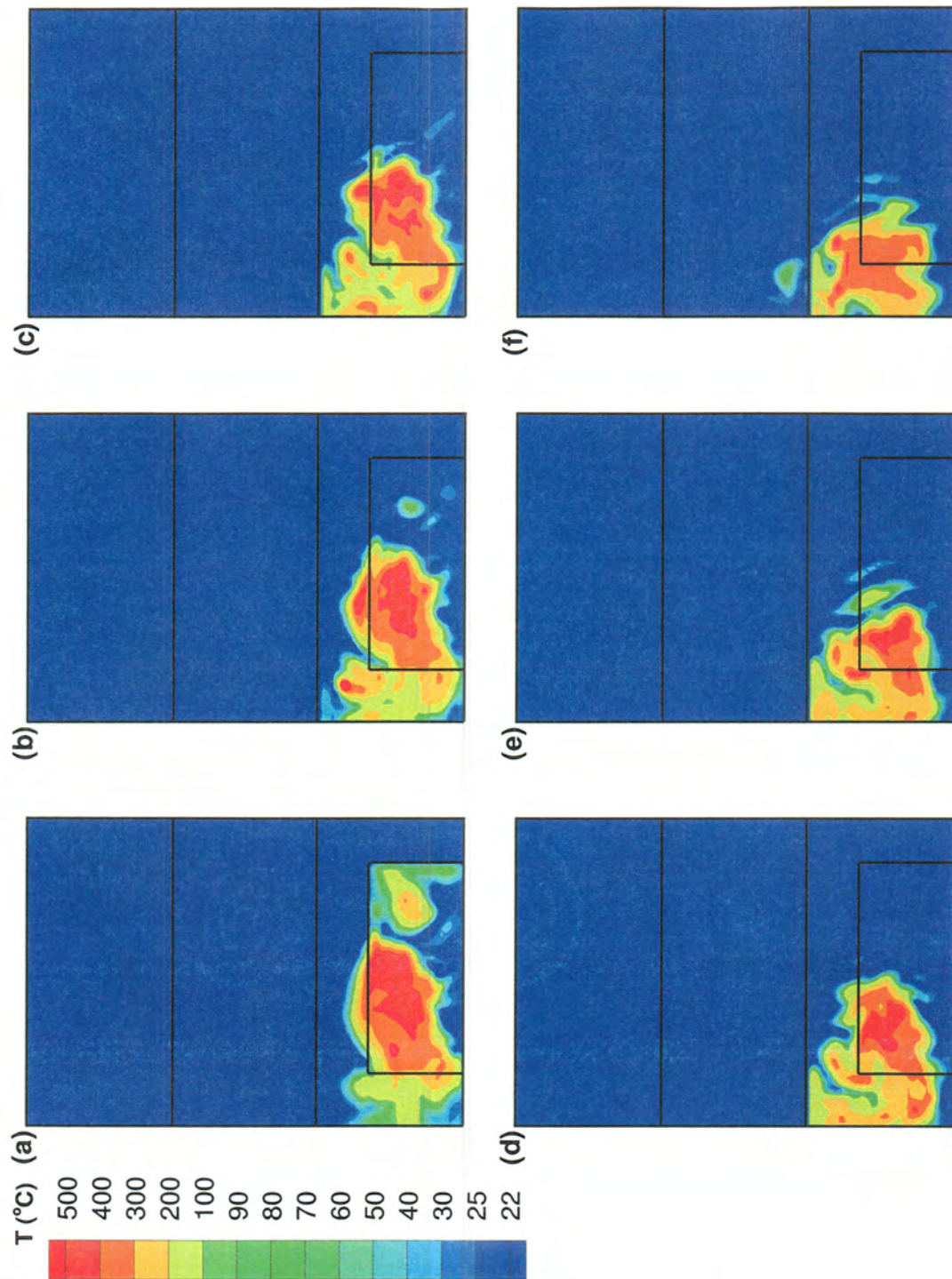


Figure 4.15 Instantaneous temperature contours at  $t=48$  s and wind angle  $\theta=45^\circ$  at locations (a)  $x=-0.015$  m, (b)  $x=-0.045$  m, (c)  $x=-0.075$  m, (d)  $x=-0.105$  m, (e)  $x=-0.135$  m and (f)  $x=-0.180$  m.

## CHAPTER 5 CONCLUSIONS

Large eddy simulation along with a mixture fraction combustion model was employed for a three-dimensional study of a balcony's effect on vertical fire spread in multi-level apartment complexes. Studies of grid-sensitivity were completed for both combustion and hydrodynamics to determine if the models were reasonably predicting the physics of fire and fluids. Scaled heat release rates were then compared to equivalent full scale heat release rates. A 48 kW fire at 1/7th scale was shown to be approximately equivalent to a 6.22 MW fire full scale, which is realistic for a similar size occupant dwelling with typical furnishings.

The numerical simulations were then compared to scale experiments by Suzuki et al. [40] for varying balcony depths from 0–20 cm (0–1.4 m full scale). The exterior building facade temperatures were recorded to indicate the threatening levels of hot gases. Radiation from the smoke and hot gases can increase the facade temperature to the point of flaming ignition, inducing vertical fire spread. The gas temperatures at the first and second floors above the fire floor (FF +1, FF +2) were similar to that from Suzuki et al. In both experiments [40] and these simulations, an increased balcony depth projects hot gas away from the facade of the building, reducing the heat flux to the surface and thus delaying vertical fire spread.

Occupants trapped on a balcony at floors above the fire floor would correspond to the lowest three thermocouple readings per floor. Time-averaged gas temperatures for a 17.5 cm balcony depth at occupant level only reach 50°C, which is survivable for a human, compared to almost 60°C for BD=15 cm. A BD=17.5 cm at 1/7th scale

was shown to be 1.225 m at full scale, which is an acceptable depth for building code standards in the U.S. and abroad.

Finally, keeping the  $BD=17.5$  cm, the effects of balcony geometry were investigated. Four different types of balconies were identified and classified. The balcony types contained different balustrade and separation wall configurations. Changing the geometry of the balcony had a measurable effect on the vertical movement of smoke and gas. A rectangular balcony, with open, non-combustible balustrades and open separation walls (Type I) provided the most protection from vertical fire spread. The hot gases were projected away from the facade, reducing the temperatures at both FF +1 and FF +2. A balcony with solid balustrades and separation walls was shown to trap the hot gases at floors above the fire floor, making it difficult for trapped occupants to survive, as well as increasing the rate of vertical fire spread.

A preliminary computational study was conducted to determine what affect wind has on high rise building fires with balconies. A Type I balcony with  $BD=17.5$  cm was implemented with a 1.5 m/s (4.1 m/s full scale) wind entering the computational domain at  $0^\circ$ ,  $10^\circ$ ,  $30^\circ$  and  $45^\circ$  where  $0^\circ$  is parallel to the facade of the building. The wind greatly changed the characteristics of the hot gas plume interacting with a balcony. Wind entering at a  $45^\circ$  angle trapped the hot gas below the FF +1 balcony, creating horizontal fire spread which is potentially hazardous to apartments adjacent to the fire room. As the wind angle was decreased from  $45^\circ$  to  $0^\circ$ , the horizontal movement of the hot gas plume increased the spread of fire to adjacent apartments.

Future work in this area could include a more detailed study of wind at other angles, such as wind impinging on the backside of the building, to evaluate the effect of balcony performance in reducing vertical fire spread. Other areas left for future research may include implementing material properties to a building itself, such that surfaces are not adiabatic but instead are combustible surfaces. Balcony geometries made from wood or other combustible materials could also be investigated.

## BIBLIOGRAPHY

- [1] Fire! Destruction of Chicago! 2,600 Acres of Buildings Destroyed., *Chicago Tribune*, (October 11, 1871).
- [2] Glanz, J., A day of terror: The Buildings; Towers Believed to be Safe Proved Vulnerable to an Intense Jet Fuel Fire, Experts Say, *New York Times*, (September 12, 2001).
- [3] Van Natta, D. and Alvarez, L., A Day of Terror: Attack on Military; A Hijacked Boeing 757 Slams into the Pentagon, Halting the Government, *New York Times*, (September 12, 2001).
- [4] U.S. Fire Administration, "Highrise Fires", *Topical Fire Research Series*, 2(18) (2002).
- [5] Morton, B. R., Modeling Fire Plumes, in *Tenth Symposium (International) on Combustion*, pp. 973–982, 1965.
- [6] Harmathy, T. Z., A New Look at Compartment Fires, *Fire Technology*, 8 (1972).
- [7] Emmons, H. W., Fire in the Forest, *Fire Research Abstracts and Reviews*, 5(3):163–178 (1963).
- [8] Albini, F. A., Wildland Fires, *American Scientist*, 72:590–597 (1984).
- [9] Emmons, H. W. and S.-J., Ying, The Fire Whirl, in *Eleventh Symposium (International) on Combustion*, pp. 475–488, 1967.

- [10] Byram, G. M. and Martin, R. E., The Modeling of Fire Whirlwinds, *Forest Science*, **16**(4):386–399 (1970).
- [11] Muraszew, A., Fedele, J. B., and Kuby, W. C., The Fire Whirl Phenomenon, *Combustion and Flame*, **34**:29–45 (1979).
- [12] Battaglia, F., McGrattan, K. B., Rehm, R. G., and Baum, H. R., Simulating Fire Whirls, *Combustion Theory Modeling*, **4**:123–138 (2000).
- [13] Madrzykowski, D. and Vettori, R. L., Simulation of the Dynamics of the Fire at 3146 Cherry Road NE, Washington D.C., May 30, 1999, Technical Report NISTIR 6510, National Institute of Standards and Technology, April 2000.
- [14] Sutula, J., The Fire Dynamics Simulator in Fire Protection Engineering Consulting, *SFPE Fire Protection Engineering*, **15**:46–51 (2002).
- [15] Byram, G. M., Scaling Laws for Modeling Mass Fires, *Pyrodynamics*, **4**:271–284 (1966).
- [16] Soma, S. and Saito, K., Reconstruction of Fire Whirls Using Scale Models, *Combustion and Flame*, **86**:269–284 (1991).
- [17] Hirano, T. and Saito, K., Fire Spread Phenomena: The Role of Observation in Experiment, *Prog. Energy Combustion Science*, **20**:461–485 (1995).
- [18] Kramlich, J.C. and Malte, P.C., Modeling and Measurement of Sample Probe Effects on Pollutant Gases Drawn from Flame Zones, *Combustion Science and Technology*, **18**(3-4):91–104 (1978).
- [19] Yanagi, T. and Mimura, Y., Effect of Concentration Gradient on Composition of Sample Gas, *Combustion and Flame*, **28**:347–356 (1972).

- [20] Nguyen, Q.V., Edgar, B.L., Dibble, R.W., and Gulati, A., Experimental and Numerical Comparison of Extractive and In Situ Laser Measurements of Non-Equilibrium Carbon Monoxide in Lean-Premixed Natural Gas Combustion, *Combustion and Flame*, **100**:395–406 (1995).
- [21] Schoenung, S.M. and Hanson, R.K., CO and Temperature Measurements in a Flat Flame by Laser Absorption Spectroscopy and Probe Techniques, *Combustion Science and Technology*, **24**(5-6):227–237 (1981).
- [22] McGrattan, K., Baum, R., H. Rehm, Hamins, A., and Forney, G., Fire Dynamics Simulator - Technical Reference Guide, Technical Report NISTIR 6467, National Institute of Standards and Technology, 2001.
- [23] Carlsson, J., Fire Modeling Using CFD - An Introduction for Fire Safety Engineers, Technical Report 5025, Department of Fire Safety Engineering, Lund University, Sweden, 1999.
- [24] Karlsson, B. and Quintiere, J., *Enclosure Fire Dynamics*, chapter 10, pp. 12,258, CRC Press, Boca Raton, Florida, 2000.
- [25] Patankar, S.V., *Numerical Heat Transfer and Fluid Flow*, Hemisphere Publishing, 1980.
- [26] Rehm, R.G. and Baum, H.R., The Equations of Motion for Thermally Driven, Buoyant Flows, *Journal of Research, National Bureau of Standards*, **83**(3):297–308 (1978).
- [27] Faraday, Michael, *The Chemical History of a Candle*, 1860.
- [28] Quintiere, J.G., *Principles of Fire Behavior*, Delmar Publishers, New York, 1998.
- [29] Brehob, E. and Kulkarni, A. K., Experimental Measure of Upward Flame Spread on a Vertical Wall with External Radiation, *Fire Safety Journal*, **31**:181–200 (1998).

- [30] Brehob, E.G., Kim, C.I., and Kulkarni, A. K., Numerical Model of Upward Flame Spread on Practical Wall Materials, *Fire Safety Journal*, **36**:225–240 (2001).
- [31] Carlsson, J. and Karlsson, B., Numerical Simulation of Fire Exposed Facades, Technical report, Department of Fire Safety Engineering, Lund University, Sweden, 2001.
- [32] North, G., Karlsson, B., Gojkovic, D., and van Hees, P., Simple Analytical and Numerical Techniques for Modeling Flame Spread on Solids, Technical report, Department of Fire Safety Engineering, Lund University, Sweden, 2001.
- [33] Bong, F., Fire Spread on Exterior Walls, Master's thesis, Dept. of Fire Engineering, University of Canterbury, New Zealand, 2000.
- [34] Carlsson, E., External Fire Spread to Adjoining Buildings, Master's thesis, Dept. of Fire Safety Engineering, Lund University, Sweden, 1999.
- [35] Yokoi, S., Study on the Prevention of Fire Spread Caused by Hot Upward Current, Technical report, Building Research Institute, Japan, Report 34, 1960.
- [36] Oleszkiewicz, I., Fire Exposure to Exterior Walls and Flame Spread on Combustible Cladding, *Fire Technology*, **26**(4):357–375 (1990).
- [37] Oleszkiewicz, I., Fire and Combustible Cladding, *Construction Canada*, **32**(4):16–18, 20–21 (1990).
- [38] Oleszkiewicz, I., Vertical Separation of Windows using Spandrel Walls and Horizontal Projections, *Fire Technology*, **27**(4):334–340 (1991).
- [39] Galea, E. R., Berhane, D., and Hofmann, N. A., CFD Analysis of Fire Plumes Emerging from Windows with External Protrusions in High Rise Buildings, in *7th*

*International Fire Science and Engineering Conference: Interflam'96*, Cambridge, England, March 1996.

- [40] Suzuki, T., Sekizawa, A., Yamada, T., Yanai, E., Satoh, H., Kurioka, H., and Kimura, Y., An Experimental Study of Ejected Flames of a High-Rise Buildings, Technical report, National Research Institute of Fire and Disaster, Japan, 2001.
- [41] Suzuki, T., Yamada, T., Sekizawa, A., Takanashi, K., Yanai, E., Abe, N., Kurioka, H., and Satoh, H., An Experimental Study on Prevention of Upward Fire Spread Caused by Hot Gas Ejected Out through Opening from Fire Room in a High-rise Apartment Building, *Fire Safety Science – 7th Int. Symp. on Fire Safety Science*, (2002).
- [42] Tannehill, J. C., Anderson, D. A., and Pletcher, R. H., *Computational Fluid Mechanics and Heat Transfer*, Taylor and Francis, 2nd edition, 1997.
- [43] Hottel, H. C., Stimulation of Fire Research in the United States After 1940, *Combustion Science and Technology*, **39**:1–10 (1984).
- [44] Forney, G. P and Moss, W. F, Analyzing and Exploiting Numerical Characteristics of Zone Fire Models, *Fire Science and Technology*, **14**(1,2):49–60 (1994).
- [45] Hamins, A., Yang, J. C., and Kashiwagi, T., An Experimental Investigation of the Pulsation Frequency of Flames, in *Twenty Fourth Symposium (International) on Combustion*, pp. 1965–1702, The Combustion Institute, 1992.
- [46] Cetegen, B. M. and Ahmed, T. A., Experiments on the periodic instability of buoyant plumes and pool fires, *Combustion and Flame*, **93**:157–184 (1993).
- [47] Mell, W.E., McGrattan, K.B., and Baum, H.R., Numerical Simulation of Combustion in Fire Plumes, in *Twenty-Sixth Symposium (International) on Combustion*, pp. 1523–1530, The Combustion Institute, 1996.

- [48] McGrattan, K.B., Baum, H.R., and Rehm, R.G., Large Eddy Simulations of Smoke Movement, *Fire Safety Journal*, **30**(2):161–178 (1998).
- [49] Baum, H. R., Rehm, R. G., and Gore, J. P., Transient Combustion in a ‘Aubulent Eddy’, in *Twenty Third Symposium (International) on Combustion*, pp. 715–722, The Combustion Institute, 1990.
- [50] Smagorinsky, J., General Circulation Experiments with the Primitive Equations. I. The Basic Experiment., *Monthly Weather Review*, **91**:91–164 (1963).
- [51] Grosshandler, W., RadCal: A Narrow Band Model for Radiation Calculations in a Combustion Environment, Technical Report TN1402, National Institute of Standards and Technology, 1993.
- [52] Continillo, G., Denaro, F.M., and Marra, F.S., Accuracy and Stability Analysis of Time-Integrated Schemes for Advection-Diffusion-Reaction Equations, in *Seventh International Conference on Numerical Combustion*, p. 99, 1998.
- [53] Green Mountain Software, Boulder Colorado, *CRAYFISHPAK User’s Guide, Cray Version 1.1*, 1990.
- [54] Baum, H. R. and McCaffery, B. J., Fire Induced Flow Field - Theory and Experiment, in *Fire Safety Science - Proceedings of the Second International Symposium*, pp. 129–148, 1989.
- [55] Neumann, B.G., *Boundary Layer and Flow Control, Its Principles and Applications*, chapter Deflection of Plane Jets by Adjacent Boundaries-Coanda Effect, pp. 232–264, Pergamon Press, 1961.
- [56] Rehm, K. B, R. G. and McGrattan, Baum, H. R., and Simiu, E., An Efficient Large Eddy Simulation Algorithm for Computational Wind Engineering: Application to

Surface Pressure Computations on a Single Building, Technical Report NISTIR 6371, National Institute of Standards and Technology, August 1999.

- [57] Naruse, T. and Hasemi, Y., Wind Effect on Fire Behavior in Compartment, Technical Report NISTIR 6588, National Institute of Standards and Technology, November 2000.
- [58] Emori, R. I. and Saito, K., A Study of Scaling Laws in Pool and Crib Fires, *Combustion Science and Technology*, **31**:217–231 (1983).